Review—Development of Highly Active and Durable Hybrid Compressive Platinum Lattice Catalysts for Polymer Electrolyte Membrane Fuel Cells: Mathematical Modeling and Experimental Work

Journal of The Electrochemical Society, 2020 **167** 054512

Review—Development of Highly Active and Durable Hybrid Compressive Platinum Lattice Catalysts for Polymer Electrolyte Membrane Fuel Cells: Mathematical Modeling and Experimental Work

Branko N. Popov,[1,z] Jong-Won Lee,[2,†] Akos Kriston,[3] and Taekeun Kim[4]

[1]*Center for Electrochemical Engineering, Department of Chemical Engineering, University of South Carolina, Columbia, South Carolina 29208, United States of America*
[2]*Department of Materials Science and Engineering, Chosun University, Gwangju 61452, Korea*
[3]*European Commission, Joint Research Center (JRC), 21027 Ispra, Italy*
[4]*Department of Chemical Engineering Education, College of Education, Chungnam National University, Daejeon 34134, Korea*

This review provides a comprehensive overview on the development of highly active and durable platinum catalysts with ultra-low Pt loadings for polymer electrolyte membrane fuel cells (PEMFCs) through a combined mathematical modeling and experimental work. First, simulation techniques were applied to evaluate the validity of the Tafel approximation for the calculation of the mass activity (MA) and specific activity (SA). A one-dimensional agglomeration model was developed and solved to understand the effects of exchange current density, porosity, agglomerate size, Nafion® film thickness, and Pt loading on the MA and SA. High porosity (> 60%) and agglomerations at high Pt loadings cause the loss of the Tafel approximation and consequently the decrease in MA and SA. A new structure parameter was introduced to estimate the real porous structure using the fractal theory. The volumetric catalyst density was corrected by the fractal dimension (measured by Hg porosimetry), which gave a good agreement with the experimental values. The loading-dependent Tafel equation was then derived, which contains both the utilization and the non-linear scaling factor. Second, activated carbon composite support (ACCS) with optimized surface area, porosity, pore size, and pore size distribution was developed. The hydrophilic/hydrophobic ratio, structural properties (amorphous/crystalline ratio), and the number of active sites were optimized through metal-catalyzed pyrolysis. Stability of ACCS and Pt/ACCS were evaluated using an accelerated stress test (AST). The results indicated that Pt/ACCS showed no significant loss of MA and power density after 5,000 cycles at 1.0–1.5 V, while the commercial Pt/C catalysts showed drastic losses of MA and power density. Finally, monolayers of compressed Pt (core–shell-type Pt_3Co_1) catalysts were structured by diffusing Co atoms (previously embedded in ACCS) into Pt. Compressive Pt lattice (Pt^*) catalysts were synthesized through an annealing procedure developed at the University of South Carolina (USC). The Pt^*/ACCS catalyst showed high initial power density (rated) of 0.174 g_{Pt} kW^{-1} and high stability (24 mV loss) at 0.8 A cm^{-2} after 30,000 cycles (0.6–1.0 V). The outstanding performance of Pt^*/ACCS is due to the synergistic effect of ACCS and compressive Pt^* lattice.

 [DOI: 10.1149/1945-7111/ab6bc6]

Manuscript submitted October 21, 2019; revised manuscript received January 6, 2020. Published February 6, 2020. *This was Paper 2192 presented at the Seattle, Washington Meeting of the Society, May 13–17, 2018. This paper is part of the JES Focus Issue on Heterogeneous Functional Materials for Energy Conversion and Storage.*

PEMFCs are attractive power sources of the future for a variety of applications, including portable electronics, stationary power, and electric vehicles. However, sluggish cathode kinetics, high Pt cost, and durability issues inhibit the use of PEMFCs for automobile applications.[1,2] A number of factors contribute to the performance degradation of PEMFCs, including catalyst dissolution,[3–8] catalyst sintering,[7,9] membrane degradation,[10–12] and carbon support corrosion.[13–16] The requirements for PEMFC lifetime significantly vary for different applications; 5,000 h for cars, 20,000 h for buses, and 40,000 h for stationary applications.[4] The recent studies on the development of supports and Pt-alloy catalysts as well as on the effect of Pt loading on the MA and SA reported in the literature are summarized below.

High-cost and limited supply of Pt together with its sluggish kinetics of oxygen reduction reaction (ORR) triggered the research and development of various Pt-alloy cathode catalysts such as Pt–Fe, Pt–Co, Pt–Ni, and Pt–Cr.[3,7–27] The enhancement in measured activity over Pt by alloying Pt with 3d transition metals is due to various factors, including the lowering of the Pt oxidation state, the suppression of Pt oxide formation,[28,29] the formation of a new electronic structure with higher Pt 5d orbital vacancies,[22] the decrease in the Pt–Pt interatomic distance and therefore a more favorable O_2 adsorption,[22] the formation of a thin Pt skin on the surface of the alloy core,[30–32] and the altered electronic structures of the topmost Pt atoms.[24,25,33]

Among various Pt alloys, the Pt–Co catalysts have attracted much attention due to their high activity and stability in an acidic environment.[18,34] Paulus et al. studied the bulk compositions of 50 and 75 at% Pt with Ni and Co as alloying elements.[23,35] In comparison to pure Pt, the results revealed a small activity enhancement of ∼1.5 times for 25 at% Ni and Co and a more significant enhancement by a factor of 2–3 for 50 at% Co. Huang et al. showed that Pt–Co alloy nanoparticles exhibit MA and SA enhancements by a factor of ∼1.3–3.2 and ∼1.2−2.2, respectively, when compared to pure Pt.[36] Antolini et al. reviewed the catalyst activity and stability and concluded that Pt–Cr and Pt–Co are more stable than Pt–V, Pt–Ni, and Pt–Fe due to their high degree of alloying and particle size.[18] Jayasayee et al. studied the activity and durability of Pt–Co, Pt–Ni, and Pt–Cu in PEMFC cathodes as a function of alloying elements in a systematic manner.[26] They showed that the performance of Pt–Co and Pt–Cu was found to be more attractive when compared to those of Pt–Ni and Pt. Mani et al. investigated the activity of dealloyed Pt–Cu, Pt–Co, and Pt–Ni in PEMFCs.[27] They found that Pt-alloys with Co and Cu are more active than Pt–Ni. The MA and SA of Pt–Co and Pt–Cu were enhanced by a factor of 3–4, compared to those of the commercial Pt/C catalyst. Pt-based catalysts dissolve during PEMFC operations when the cathode is subjected to potential cycling. Pt dissolution occurs in narrow potential and pH windows near 1.0 V vs reversible

†Present address: Department of Energy Science and Engineering, DGIST, Daegu 42988, Korea
zE-mail: popov@cec.sc.edu

hydrogen electrode (RHE).[37–42] A kinetic model developed by Darling and Meyers indicates that Pt dissolution in PEMFCs is negligible at low and high potentials but significantly large at intermediate potentials.[39]

Recently, several new methods were developed to synthesize various PtCo alloy catalysts for ORR. Li et al. reported a hollow Pt_3Co alloy nanospheres formed by acid treatment after synthesis of a Co core–PtCo shell catalyst. The Co core was prepared by a wet chemical method, while the Pt_3Co shell was deposited by spontaneous galvanic displacement reaction.[43] The resulting hollow Pt_3Co catalyst with ultra-thin Pt shell (∼0.8 nm) showed 4–8 times higher activity than Pt/C and enhanced stability for 5,000 cycles between 0.6 and 1.0 V. Takahashi et al. studied synchronous arc-plasma deposition of Pt and Co and the voltammetric dealloying behavior of the Pt–Co and N-introduced Pt–Co nanoparticles.[44] The preferential multi-layered Pt-rich shell/Pt–Co core formation was achieved by the voltammetric dealloying by introducing N atoms into the Pt–Co core. The N-introduced, dealloyed Pt–Co catalyst showed 1.6 times higher ORR activity than the dealloyed Pt–Co catalyst without N. Jung et al. proposed a selective modification of the surface Co atom with N-containing polymers for Pt–Co catalysts for ORR.[45] The N-containing carbon black was used as a support material for Pt–Co catalysts, and the N group selectively interacted with Co. The electronic ensemble effects between Pt and Co–N_{surf} enhanced the ORR activity of the catalyst. The catalyst also showed a high resistance against Co oxidation, resulting in the high durability during AST.

Yang et al. investigated Pt–Co nanowire networks by a surfactant-assisted soft template synthesis method.[46] The catalyst showed enhanced initial performance of 210% MA and 220% SA as well as improved durability under AST, when compared with a commercial Pt/C catalyst. Vorokhta et al. prepared a Pt–Co thin film catalyst by co-sputtering and deposition, followed by a vacuum annealing, which enables an easier way to synthesize Pt–Co catalysts without a wet chemical method.[47] They have studied the catalyst's durability during AST using in-situ electrochemical atomic force microscopy.[48] In combination with ex-situ spectroscopic analyses, it showed detailed steps of the degradation mechanisms. Choi et al. studied a one-pot chemical vapor deposition as a facile synthetic process for mono-dispersed Pt–Co catalysts.[49] The method is suitable for practical large-scale process due to the rapid process, easy control over binary composition, and strong interaction between catalytic metals and supports. The catalyst obtained from this method showed good uniformity and dispersion even after long-term operation. Based on the catalyst durability studies available in the literature, it is evident that pure Pt-based catalysts are not stable under PEMFC operating conditions and Pt degradation occurs through agglomeration, Pt dissolution/re-deposition by Ostwald ripening mechanisms, detachment of the catalyst particles from carbon support, hydrogen crossover and hydroxide ion adsorption on Pt surface.

This review provides a comprehensive overview of research efforts at USC to develop highly stable and kinetically active support and compressive Pt catalysts through a better understanding of the effects of structures and Pt loading on the performance of PEMFCs. The hybrid technology developed at USC is based on a three-step process. In the first step, a combined experimental and simulation technique was used to evaluate the validity of the Tafel approximation used to calculate MA and SA. Comprehensive experimental characterizations of membrane–electrode assemblies (MEAs) were carried out at different Pt loadings. A combined experimental and model-based parameter estimation was employed to separate the kinetic and mass transport resistances and to evaluate the performance of the catalysts.

In the second step, cathode catalyst supports were developed by addressing the following constraints: the support should be chemically and electrochemically stable at high potentials, low pH, and high temperatures; and the ORR onset potential and kinetic activity of the support should be similar to that of Pt. High-surface area carbon (HSAC) is widely used as a catalyst support to improve Pt utilization due to its good electrical conductivity, pore structure suitable for Pt anchorage, high surface area for uniform Pt particle dispersion, easy availability, and low cost. However, many studies have shown that HSAC has low resistance against thermal and electrochemical oxidation because of the HSAC structure containing mainly amorphous carbon and small potion of plane graphite carbon that has abundance of dangling bonds and defects. The dangling bonds can easily form surface oxides, which results in a higher corrosion rate under electrochemical oxidation. HSAC, when used as supports in PEMFCs, is susceptible to corrosion due to presence of high water content, low pH (≲1), high temperature (70 °C–80 °C), high oxygen concentration and very high potentials (1.2–1.5 V vs RHE) at the cathode interface during start-up/shut-down cycles and fuel starvation. HSAC oxidation results in: (i) an increase in hydrophilic properties at the cathode interface, which affects water removal and in turn increases mass transport losses; (ii) a decrease in the catalyst layer (CL) thickness, resulting in an increase of the cell resistance; and (iii) an increase in the carbon corrosion rates due to a catalytic role of Pt. The support corrosion contributes the catalyst stability to decrease during cycling due to agglomeration, dissolution/redeposition, detachment of the catalyst particles, hydrogen crossover, and OH^- adsorption on the catalyst surface. Thus, the hydrophilic/hydrophobic ratio of the support, its structural properties (amorphous/crystalline ratio), and the number of active sites formed on the support are critical when engineering and synthesizing highly active and stable hybrid catalysts.

The hybrid catalysts in this study were engineered by considering the civil engineering principles: a stable structure's roof (catalyst) must be built on a stable foundation (support). The ACCS is synthesized using a novel methodology developed at USC. The catalyst deposited on ACCS shows no loss of MA and maximum power density after 5,000 cycles at 1.0–1.5 V.[50–53] The activity and excellent stability of the catalyst was attributed to the high degree of graphitization and enhanced hydrophobicity of the support. For the first time, we reported a carbon-based support that is stable under simulated start up/shut-down operating conditions. The active sites for ORR in the support are pyridinic-N and quaternary-N.[52,54–59] The high activity of the catalysts is ascribed to the synergetic effect of highly stable supports combined with increased activity of compressed Pt^* catalyst[51–53,60] and the presence of increased Pt^o concentration on the catalyst surface, which indicated that the pyridinic-N (a catalytic site on the activated support) played a role of oxide-cleanser, which was confirmed by physico-chemical and electrochemical analyses.[11,61]

The support was synthesized with optimized surface area, porosity, pore size, and pore size distribution. The hydrophilic/hydrophobic ratio of the support, its structural properties (amorphous/crystalline ratio), and the number of active sites formed on the support are critical when engineering and synthesizing a highly active and stable hybrid catalysts. A novel process was developed to encapsulate the transition metal in the graphitic carbon structure of the support.

In the third step, a compressive Pt lattice (Pt^*) catalyst was synthesized by using an annealing procedure that controls the particle size of the catalyst. Monolayers of Pt^* were structured by diffusing Co atoms (previously embedded in ACCS) into Pt. Procedures were developed to optimize the Co diffusion time in the catalyst, annealing temperature, and Pt/Co stoichiometric ratio. The results from the theoretical work were used to optimize experimentally the thickness of the CL, MA, SA, as well to optimize the effects of exchange current density, agglomeration size and Pt loading on the MA and SA. The loading dependent Tafel equation which contains both the utilization and the nonlinear scaling factor were used when developing experimentally a highly active and low Pt loading catalyst for PEMFCs.

Impact of Ultra-low Pt Loading on the Mass Activity and Specific Activity—Better Understanding of the Effect of the Microstructure on the Catalyst Performance

MA is defined as the current density measured at 0.9 $V_{iR\text{-corrected}}$ and normalized by the mass loading.[62,63] It is frequently applied for the comparison of the activity of different catalysts in fuel cells.[1,27,64–66] In spite of the broad application of MA, there are still uncertainties regarding how materials and experimental parameters influence the measured values. MA and SA were first applied to characterize the technical activity of the dispersed Pt particles in phosphoric acid fuel cells.[67,68] The analysis of nano-scale effects on the catalyst activity at low and high currents[62,68–70] revealed the influence of catalyst–support interactions,[71–73] support surface area,[74,75] CL thickness,[76,77] and diffusion profiles.[78,79] Particularly, a maximum of MA was found at 3–5 nm Pt particle sizes. It was assumed that the small particles have a larger amount of low-coordination Pt atoms that may increase the strength of adsorption of surface oxide species.[62] Watanabe et al. showed that the inter-crystallite distance is also an important factor,[74] which can cause a similar relationship in MA as it was found by Peuckert et al.[68] Recently, density functional theory calculation showed that OH^- is more strongly adsorbed at steps, edges, and kinks of the Pt particles. Consequently, the contribution of these under-coordinated Pt sites to the ORR is negligible.[69] Nesselberger et al. compared six different commercial Pt catalysts having different particle sizes that were deposited on the same support, and they found no particle size effect in the range of 1–5 nm; on the other hand, the effect was noticeable in the range of 5–30 nm.[70]

Gasteiger et al. studied the dependence of PEMFC performance at three different Pt loadings (0.4, 0.24, and 0.15 mg_{Pt} cm^{-2}) and concluded that the MA and electrochemical active surface area (ECSA) of a catalyst-coated membrane (CCM) were essentially independent of the Pt loading.[60] However, Saha et al. found that the utilization of a screen-printed CCM decreased as the CL loading increased from 0.02 to 0.12 mg cm^{-2}.[77] Lee et al. observed that the MA measured in MEAs was only 10%–30% of the value measured using rotating disk electrode (RDE) experiments, and it increased as the catalyst loading decreased while the utilization remained unchanged.[76] They concluded that O_2 may access the catalyst particles more effectively when it exhibits a thin-layer geometry or higher porosities at lower catalyst loadings. Debe concluded that the enhanced ORR activity of the nanostructured thin film (NSTF) 3M catalysts is a result of asymmetrical surface area distribution.[75] The asymmetrical surface area controls the gas velocity distributions in the Knudsen regime, which results in an additional pre-exponential scaling factor in the Butler-Volmer equation (dependent on a distance metric describing the catalyst surface area distribution). The catalyst loading influenced the surface enhancement factor (SEF) and consequently the scaling factor.

Siddique et al. developed a CL microscopic model mimicking the experimental fabrication of the CL.[80] The variation of the number of agglomerates changed the ECSA due to reduced connectivity and increased isolation. Large agglomerates correspond to insufficient mixing of ionomer and Pt/C and consequently limit the triple-phase boundaries (TPBs). Too small agglomerate sizes may lead to the loss of connectivity or entanglement between them. According to recent studies,[1,50,66,81–87] the electrode fabrication method has a profound effect on the optimal Pt loading and utilization and therefore the measured MA. Numerous studies were performed, but no final agreement has been achieved regarding what factors characterize MA and SA, even in flooded agglomerates,[62,74] and what experimental conditions are necessary.[69,70] Thus, to develop an ultra-low, highly active and durable hybrid catalysts, our initial focus was to study both MA and SA in detail for a better understanding of the effects of the catalyst loading on these parameters.

Figure 1 shows the hydrogen adsorption and desorption peaks in the cyclic voltammograms recorded for different Pt loadings in 25 cm^2 MEAs.[63] The catalyst inks used in the MEAs were prepared

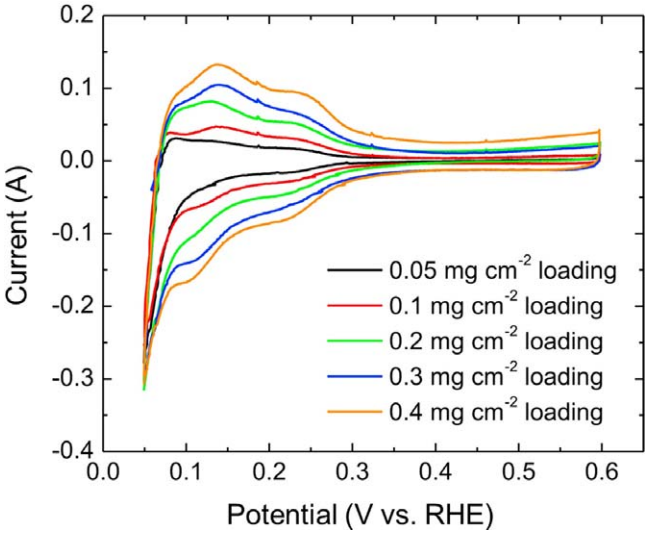

Figure 1. The cyclic voltammetric measurements of MEAs at different Pt loadings. Anode: 100% H_2 200 ccm; cathode: 100% N_2 75 ccm; cell temperature: 80 °C; 100% RH. Reprint from permission from Ref. 63; Copyright 2013, Elsevier.

by ultrasonically mixing 46% Pt/C catalyst synthesized at USC.[88] The ionomer in the catalyst ink was maintained at 30 and 20 wt% for the anode and cathode, respectively. The cathode catalyst ink was sprayed directly on a Nafion® 212 membrane, and the anode was sprayed on a gas diffusion layer (GDL, SGL 10 BC). Finally, the cathode CCM was sandwiched between the catalyst coated GDL (anode) and bare GDL. The total charge for the hydrogen adsorption/desorption increased as the Pt loading increased in the MEA. As expected, the current in the double-layer region also increased with an increase in the Pt loading. The ECSA of Pt was calculated by integrating the charge under hydrogen desorption peaks at 0.05–0.35 V vs RHE.[89,90,91,92] The charge required for the desorption of a monolayer of H^+ on a planar Pt electrode surface was assumed to be 210 mC cm^{-2}.[89] As shown in Table I, the ECSA decreased with an increase in the Pt loading, while a thin-layer RDE method revealed that the ECSA was 85 m^2 g^{-1},[88] which was very close to the theoretically expected value. The higher ECSA values at lower Pt loadings may be attributed to the fact that the Pt particles are uniformly distributed at a thin CL on the Nafion® membrane with minimum particle agglomeration. This increases the availability of active sites for ORR, resulting in maximum catalyst utilization. Table I also demonstrates that the catalyst utilization for different MEAs decreased from 82% to 48% when the Pt loading was increased from 0.05 to 0.4 mg_{Pt} cm^{-2}.

The utilization of the Pt catalyst depends on how effectively the catalyst particles are connected to the ionic conductor (Nafion® membrane) and the electronic conductor (gas diffusion layer, GDL). If the thickness of the CL increases, the probability of the percolation of the reactants through the CL may decrease. Hence, the reactants may not reach the Pt catalytic sites that are far away from the Nafion® membrane/GDL interface, resulting in lower catalyst utilization at higher Pt loadings.

Figure 2 shows the effect of Pt/C loading on the polarization behavior. The fuel cell was operated at 80 °C under H_2/O_2, 100% relative humidity (RH), and ambient pressure.[63] The MA was determined using the experimental conditions suggested by the U.S. DRIVE Partnership, Fuel Cell Technical Team Cell Component Accelerated Stress Test and Polarization Curve Protocols for Polymer Electrolyte Membrane Fuel Cells.[73] In both high (Fig. 2a) and low (Fig. 2b) current regions, the current density increased as the loading increased, but the increase was more substantial when the loading increased from 0.05 to 0.2 mg cm^{-2}.

Table I. Comparison of the electrochemical properties for different Pt loadings.

Pt loading (mg cm^{-2})	ECSA (fuel cell/RDE) (m^2 g^{-1})	Utilization (%)	Current density @0.9V$_{iR\text{-corrected}}$ (A cm^{-2})	MA (mA mg$_{Pt}^{-1}$)	SA (μA cm$_{Pt}^{-2}$)	Tafel-slope (V dec^{-1})
0.05	70/85	82	0.012	240	328	−0.065
0.1	68/85	79	0.0185	185	261	−0.065
0.2	64/85	58	0.03	150	296	−0.063
0.3	48/85	56	0.0321	107	218	−0.064
0.4	41/85	48	0.035	87.5	209	−0.063

As expected, the current density measured at 0.9 V$_{iR\text{-corrected}}$ decreased from 35 to 12 mA cm^{-2}.

The MA, SA, catalyst loading, ECSA, or SEF can be calculated if three of the five parameters are known by using Eqs. 1–3:

$$MA = \frac{i_{0.9V}}{m_{Pt}} \quad [1]$$

$$SA = \frac{i_{0.9V}}{m_{Pt} \cdot ECSA_{MEA}} \quad [2]$$

$$SEF_{MEA} = ECSA_{MEA} \cdot m_{Pt} \quad [3]$$

where $i_{0.9\ V}$ is the current density measured at 0.9 V$_{iR\text{-corrected}}$ and normalized to the geometrical surface area, and m_{Pt} is the Pt loading. In general, MA is evaluated by the Tafel equation. This equation is valid under the assumption that the surface area of the individual particles can be linearly added and is linearly proportional to the mass of the catalyst:

$$\eta = TS \log(j_{cell} + j_{H_2}) - TS(ECSA \cdot m_{Pt} \cdot j_0) \quad [4]$$

where η is the overpotential, TS is the Tafel slope, j_{cell} is the measured total cell current density, and j_{H_2} is the hydrogen crossover current density (3.3 mA cm^{-2}). The value of j_{H_2} can vary depending on the experimental conditions.

Equation 4 requires that the following should yield identical slopes: $E_{iR\text{-corrected}}$ vs $\log\left(\frac{j_{cell} + j_{H_2}}{m_{Pt}}\right)$ or $E_{iR\text{-corrected}}$ vs log (MA). With this assumption, the cathode performance is controlled only by the ORR kinetics and the ohmic losses (R_Ω), or:

$$\left[\frac{\Delta E_{iR-free}}{\Delta \log(i_m)}\right]_{p_{O_2}, p_{H_2}, T, A_{Pt,el}} = -TS \quad [5]$$

Figures 3a and 3b show the SA and MA, respectively, at different Pt loadings.[63] An increase of MA up to 230 mA mg$_{Pt}^{-1}$ was observed for 0.05 mg cm^{-2}, compared with the MA of 85 mA mg$_{Pt}^{-1}$ measured for 0.4 mg cm^{-2}. As shown in Table I, the MA increased when the loading decreased, which is in agreement with the prediction of Eq. 4. The observed increase of the MA may be related to the increase in ECSA from 41 to 70 m^2 g^{-1} in Table I. The ECSA increase is a consequence of the catalyst utilization. The effect of the ECSA can be evaluated, by substituting the current density with the specific current. The results in Table I show that the SA increased from 209 to 328 μA cm$_{Pt}^{-2}$ when the loading decreased from 0.4 to 0.05 mg cm^{-2}. The MA and SA increased by a factor of 2.7 and 1.6, respectively, while the ECSA increased to 1.7 times of its original value. This implies that the ECSA partially accounted for the increase in MA. Consequently, the structure of the active layer or the reaction path may have also changed. Inaba et al. showed that the increase of Pt loading altered the agglomeration of Pt/C on an RDE disk.[72] Bonakdarpour et al. varied the loadings of the NSTF catalysts and found that the reaction mechanism of the ORR changed.[73] The lower loadings or increased catalyst agglomeration altered the reaction path of the ORR, which was attributed to the sparsely distributed active sites. The slopes of the log i_{Pt}–V and log i_m–V plots were almost identical to the theoretically expected values for the different Pt loadings, which indicates that the MEAs were kinetically controlled and the reaction path did not change. Consequently, the increased MA points out that the MA curves cannot be reasonably predicted by Eq. 4; therefore, the polarization curves obtained for 46% Pt/C catalyst cannot be fitted with Eq. 4. According to the experimental results, the MA is controlled not only by R_Ω and the ORR kinetics, but also by the utilization of the Pt surface area, which in turn depends on the Pt loading shown in Table I. The MA is also controlled by the morphology of the CL, which depends on the

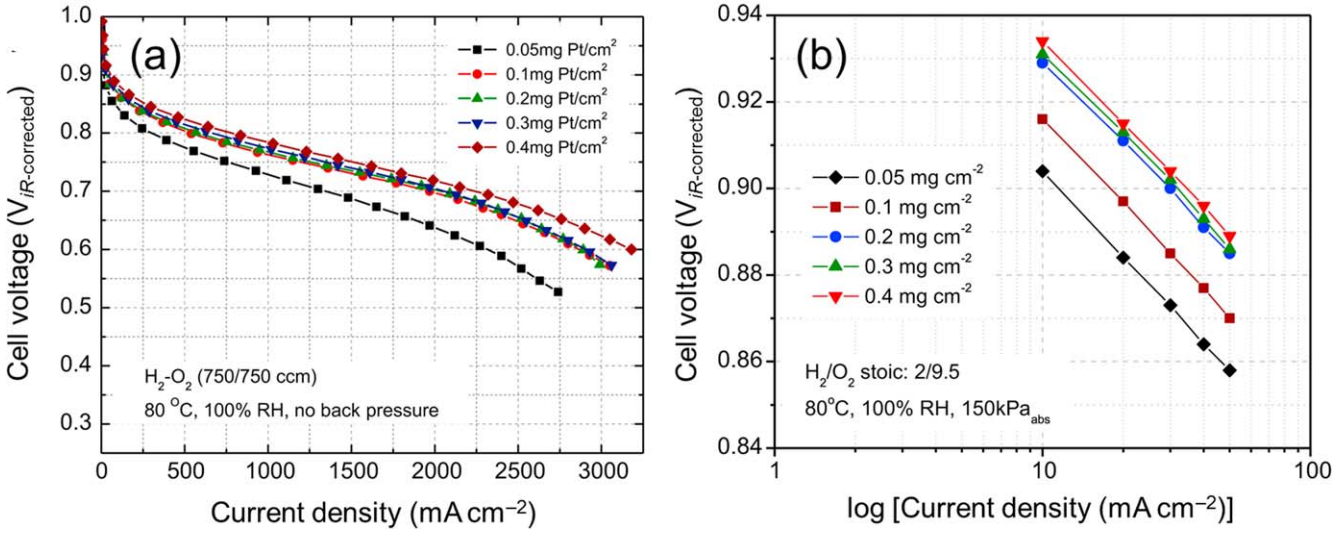

Figure 2. Effects of the Pt loading on the H_2/O_2 fuel cell performance at (a) high and (b) low current regions. Reprint from permission from Ref. 63; Copyright 2013, Elsevier.

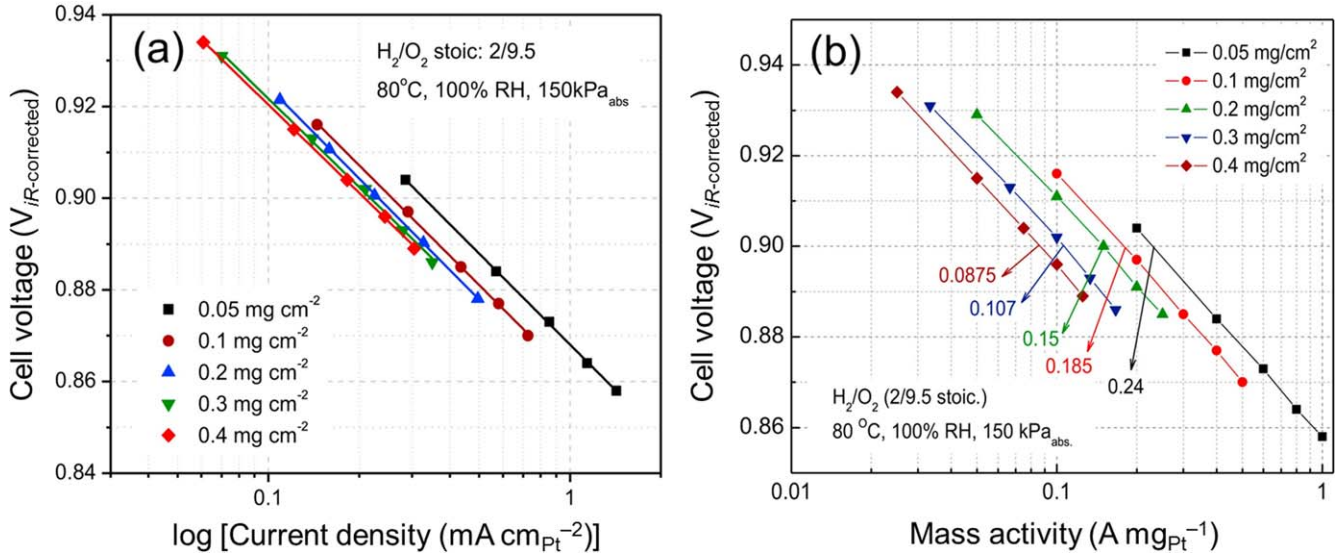

Figure 3. Effect of the Pt loading on the (a) SA and (b) MA of MEAs under the Department of Energy (DOE) fuel cell operation conditions. Reprint from permission from Ref. 63; Copyright 2013, Elsevier.

self-assembled nature of the catalyst and how effectively it fills out the volume.

Table II presents the microstructural properties of the CLs at different loadings. The data clearly show that the loading highly influenced the physical properties of the CL. The specific surface area decreased from 754 to 212 $m^2\ g^{-1}$ as the loading increased from 0.05 to 0.4 g cm^{-2}. This suggests that the newly deposited particles stick to the previous ones and screen each other's surfaces. At 0.05 mg cm^{-2}, the pore size between the agglomerates was ~12 nm, but at 0.4 g cm^{-2}, it shifted to ~40 nm. Simultaneously, the pores smaller than 20 nm diminished. The porosity was almost the same, 39% and 42% at 0.05 and 0.4 mg cm^{-2}, respectively. At 0.05 g cm^{-2}, the porosity showed a higher value (39%) than that (31%) for 0.1 g cm^{-2}, probably because the particles first coated the membrane, and after 100% coverage, they started to overlap with the previous layers. Above 0.1 mg cm^{-2}, an increasing trend was clearly shown from 31% to 47% as the loading increased from 0.1 to 0.4 mg cm^{-2}.

The results can be explained by taking into account that in PEMFCs, the catalyst forms TPBs in a three-dimensional (3D) structure of gas, catalyst, and electrolyte, which makes the experiments and the evaluation of the data more complex than for simply flooded agglomerates.[62] Agglomerate and macro-homogeneous models have been developed to model the polarization curves. However, they have no general solutions; different asymptotic solutions have been derived. One of the first solutions was developed by Perry et al.[93] When both diffusion and proton migration are not limiting (as in the kinetic region), the following expression can be derived:

$$i = -i_0 a_{Pt}\left(\frac{c}{c_0}\right) l_{CL} \exp\left(-\frac{RT}{\alpha F}\eta^c\right) \quad [6]$$

where a_{Pt} is the area of the active catalyst per unit volume ($cm^2\ cm^{-3}$), i_0 is the exchange current density, l_{CL} is the CL thickness (theoretical value), T is the temperature, R is the universal gas constant, α is the symmetry factor for the charge transfer, c is the oxygen concentration at the catalyst interface, and c_0 is the reference concentration. This model, however, does not take the Pt loading into consideration.

Jaouen et al. developed a spherical agglomerate model and also determined the asymptotic solutions.[94] In the kinetic region, it was found that

$$i = -i_0 a_{Pt}\left(\frac{c}{c_0}\right) l_{CL}(1-\varepsilon_1)(1-\varepsilon_2)\exp\left(-\frac{RT}{\alpha F}\eta^c\right) \quad [7]$$

where ε_1 is the polymer volume fraction inside the agglomerate and ε_2 is the gas-phase porosity (macroporosity). In their model, the current depends on the structure of the active layer. The general theory of dimensionless analysis and asymptotic solutions were developed by Gyenge,[95] but in the kinetic region, he derived the same relationship as outlined in Eqs. 4 and 5.

The Pt active area per unit volume is commonly determined by

$$a_{Pt} = \frac{m_{Pt}\nu_{Pt} ECSA_{RDE}}{W_{CL}} \quad [8]$$

where $ECSA_{RDE}$ is the specific ECSA of the catalyst ($m^2\ g^{-1}$) measured using a thin-layer RDE and ν_{Pt} is the catalyst utilization.[96–98] The thickness (W_{CL}) can be calculated by assuming the conservation of volume. This model indicates that the ECSA and the structure are independent of the loading and consequently leads to the same linear scaling approach between the loading and the volumetric specific surface area as the Tafel approximation, i.e., a_{Pt} is independent of the loading. Contrarily, Lin et al. concluded that Pt and C act as the structural element, while the ionomer essentially fills out the voids.[99] Pt particles smaller than 1.7 nm are mainly incorporated into the pores, but bigger particles (3–5 nm) are mainly found on the surface. Zhang et al. also concluded that Pt particles are in

Table II. Physical characterization and pore structure of the catalyst layer at different Pt loadings.

Pt loading (mg cm^{-2})	Specific surface area ($m^2\ g^{-1}$)	Agglomerate radius (nm)	Pore diameter (nm)	Porosity (%)	Surface fractal dimension (–)
0.05	754	39.7	12	39	2.937
0.1	557	58.3	11	31	2.898
0.3	244	102	44	34	2.763
0.4	212	135	39	43	2.722

the mesopores and Nafion® is primarily present on the external surface, blocking the micropores but not the macropores.[100] Gode et al. studied the effects of Nafion® loading by using different porosimetry and simulation techniques.[101] They observed that the increase in Nafion® loading did not increase the layer thickness linearly. Nafion® first covered the micropores (< 10 nm) and later the macropores (> 10 nm). These result indicate that the volume and the thickness depend on how the CL was formed and how the particles were connected to each other, and how they filled out the volume. Therefore, Eq. 8 should be precisely calculated as the quotient of the total surface area of the catalyst (A_{tot}) and the total volume of the CL (V_{tot}):

$$a_{Pt} = \frac{A_{tot}}{V_{tot}} = \frac{ECSA \cdot M_{Pt}}{V_{tot}} = ECSA(M_{Pt}) \cdot \rho_{Pt}(M_{Pt}) \quad [9]$$

where M_{Pt} is the total Pt loading (mg) and $\rho_{Pt}(M_{Pt})$ is the loading-dependent Pt density (mg cm^{-3}) in the agglomerates or in the CL. Equation 8 is valid only if the ECSA and ρ_{Pt} are to be independent of the loading. However, the measured data, shown in Table I, indicate that the ECSA depends on the loading. The CL may also depend on the loading, which was summarized previously according to Refs. 73, 93, 94 Introducing a non-linear scaling factor, like to the utilization of the ECSA (Table I), Eq. 9 can be rewritten into the following form:

$$a_{Pt} = ECSA \cdot \nu_{MEA} \rho_{Pt} P_{MEA} \quad [10]$$

where ν_{MEA} is the catalyst utilization (%) of the MEA at different loadings and P_{MEA} is the non-linear scaling factor (%). While ρ_{Pt} now does not depend on the loading, it can be calculated by dividing it with the geometrical surface area:

$$\rho_{Pt} = \frac{M_{Pt}}{V_{CL}} = \frac{m_{Pt}}{W_{CL}} \quad [11]$$

and Eq. 8 becomes

$$a_{Pt} = ECSA \cdot \nu_{MEA} \frac{m_{Pt}}{W_{CL}} P_{MEA} \quad [12]$$

W_{CL} is the average thickness predicted by the spherical agglomerate model. The real thickness of the CL is very difficult to determine by scanning transmission electron microscope (STEM) measurement, because the surface of the CL is very rough (non-uniform).

The combination of the asymptotic solutions of the macro-homogeneous and agglomerate models (Eqs. 6 and 7) and the new form of the surface area per unit volume of the cathode CL (Eq. 12) renders the log *i*–V relationship with the following general form:

$$\eta_0 = TS \ln\left[\frac{j_{cell}}{ECSA \cdot \nu_{MEA} i_0 P_{MEA} m_{Pt}} \left(\frac{c^{O_2}_{REF}}{c^{O_2}_{GDL}}\right)^{\gamma}\right] \quad [13]$$

Substituting $\frac{j_{cell}}{m_{Pt}} = i_m$ with the mass specific current and using the log identities, we reach

$$\eta = TS \ln(i_m) - TS \ln\left(ECSA \cdot \nu_{MEA} i_0 P_{MEA} \left(\frac{c^{O_2}_{GDL}}{c^{O_2}_{REF}}\right)^{\gamma}\right) \quad [14]$$

Also including $\frac{j_{cell}}{ECSA \cdot \nu_{MEA} m_{Pt}} = i_{Pt}$, we get

$$\eta = TS \ln(i_{Pt}) - TS \ln\left(i_0 P_{MEA} \left(\frac{c^{O_2}_{GDL}}{c^{O_2}_{REF}}\right)^{\gamma}\right) \quad [15]$$

which are both Tafel-type equations; however, the constants are different from the original Tafel equation. It is evident that the non-linear scaling factor influences both MA and SA.

Analysis of the Effect of Ultra-low Pt Loading on the Mass Activity and Specific Activity in PEMFCs

Popov et al. studied the dependence of MA on the Pt loading by analytical and numerical calculations.[102] The objective was to evaluate the validity of the commonly applied Tafel approximation on the MA. An attempt was made to incorporate the fractal dimension (measured by Hg porosimerty) into the spherical agglomerate model to explain the variation of the utilized electrochemical surface area per unit volume with the catalyst loading. The fractal dimension was determined by using the built-in function of the equipment and the following relation[103]:

$$\log(V) = (2 - D_f) \log(p - p_{threshold}) + A \quad [16]$$

where V is the specific intrusion volume, D_f is the fractal dimension, $p_{threshold}$ is the pressure where the fluid percolates the first time, i.e., the intrusion volume vs pressure is the steepest, and A is a proportionality constant. The agglomerate size (r_{agg}) was calculated by using the method of Ihonen et al. according to the following formula[104]:

$$r_{agg} = \frac{3}{S_{agg} \rho_{agg}} \quad [17]$$

where S_{agg} and ρ_{agg} are the measured surface area and density of agglomerates, respectively.

The surface fractal dimension shows a continuous decrease as the loading increases in Table II. Fractal dimension can be measured by applying different yardsticks for the measurement of a geometric property, i.e., length, surface, mass, and volume. The proportionality factor between the applied yardstick and the measured quantity is the fractal dimension. For non-fractal objects, the fractal dimension is equal to the embedded Euclidean dimension. Void can be also measured between the particles. It is not evident, even if for the same object, that the void and the mass have the same fractal dimension, though it is intuitively expected. In the case of Menger-sponge, the void is not at all a fractal. There exist surface fractals whose fractal dimension measures how well the surface fills the surrounding shape. The surface fractal dimension is between 2 and 3. If it is closer to 3, it means that the matter fills out the volume very effectively, while if it tends to 2, the object is closer to a 2D (flat) surface. The result of the analysis of the fractal dimension indicates that, as the loading increases, the particles fill out the volume of the CL less effectively, due to the agglomeration and screening effects.[105,106] Fractal dimension can be measured directly by using scattering techniques or Hg porosimetry, which may add only one more parameter to the model. Percolation networks are also fractals that are commonly applied for the calculation of the transport properties in the CL.

Model development.—An agglomerate model nested in the macro-homogeneous model was used assuming small overpotentials between 0.95 and 0.85 V vs standard hydrogen electrode (SHE) where the current densities are small: (i) the ohmic loss in the carbon is negligible; (ii) O_2 diffusion in the macropores is negligible; (iii) humidity is constant and flooding does not occur; and (iv) isotherms and one dimensional model are applied (no channel effects). The simplified partial differential system is

$$\frac{dj}{dx} = -a_{Pt} i_0 S(\eta); \quad \frac{d\eta}{dx} = -\sigma_{Nafion} j; \quad j(0) = j_{cell}; \quad j(W_{CL}) = 0 \quad [18]$$

where $S(\eta)$ is a general electrochemical reaction, σ_{Nafion} is the effective Nafion® conductivity, and j is the proton current density. Applying the method of Kulikovsky for the solution of Eq. 18, one can reach the dimensional form of the penetration depth[107]:

$$\upsilon = \sqrt{\frac{RT\sigma_{\text{Nafion}}}{2\alpha nFa_{\text{Pt}}i_0W_{\text{CL}}^2}} \quad [19]$$

where n is the number of electrons involved. The penetration depth is the key indicator that determines if the asymptotic solution is valid and also indicates the dependence of MA on the Pt loading.[94,95] It specifies whether the reaction profile is uniform, and whether all the catalysts are exposed in the same way. Thus, the penetration depth will be expressed by the Pt loading.

The Pt active area per unit volume is determined by Eq. 8. Some of the models reported in literature considered the length as an input experimental parameter,[93,94,97] and the porosity (P) and the volume fraction of the void spaces (ε_{V}) were calculated by the following equation:

$$P = \frac{1}{1-\varepsilon_{\text{V}}} = \frac{W_{\text{CL}}}{L_0} \quad [20]$$

where L_0 is the thickness of the CL without any void space. Other models considered the Pt loading and porosity as an input, because during the CL preparation, the catalyst loading is the main control parameter.[96,108,109] In this case, the thickness of the CL can be calculated by using the following expression:

$$W_{\text{CL}} = P\sum_i \frac{m_{\text{i}}}{\rho_{\text{i}}} = P\cdot m_{\text{Pt}}\sum_i \frac{m_{\text{i}}/m_{\text{Pt}}}{\rho_{\text{i}}} = P\cdot m_{\text{Pt}}Y_0 \quad [21]$$

where m_{i} is the mass per unit area of the ith material (i.e., Pt, carbon, Nafion®), ρ_{i} is the density of the ith material, and Y_0 is related to the composition of the layer.

The Bruggman relation is commonly applied for the calculation of transport properties in the porous structure. The ionic conductivity can be expressed as

$$\sigma_{\text{Nafion}} = \sigma_{\text{bulk}}\varepsilon_{\text{Nafion}}^{1.5} \quad [22]$$

while the diffusion coefficient is

$$D_{\text{eff}} = D_{\text{bulk}}\varepsilon_{\text{V}}^{1.5} \quad [23]$$

where $\varepsilon_{\text{V}} = 1-(\sum\varepsilon_{\text{i}})$ and

$$\varepsilon_{\text{i}} = \frac{m_{\text{i}}}{\rho_{\text{i}}W_{\text{CL}}} \quad [24]$$

where ε_{i} is the volume fraction of the ith material. All of the previous models neglected any structural variation in the CL if the loading or the composition (Nafion® content) varied. All the models considered a linear relationship among the mass loading, the volume, the thickness of the CL and the agglomerate density. Thus, the validity of the linearity was assumed, and later a different metrics was proposed by using the fractal dimension.

The validity region of the Tafel approximation.—The dimensional form of the penetration depth (Eq. 19) by using the structural characterizations (Eqs. 8 and 20–24) is

$$\upsilon = \frac{1}{m_{\text{Pt}}}\sqrt{\frac{RT\sigma_{\text{Nafion}}(1-\varepsilon_{\text{V}})}{2\alpha F\cdot ECSA_{\text{RDE}}\nu_{\text{MEA}}i_0Y_0}} \quad [25]$$

If the penetration depth is $\upsilon > 1$, it means that the reaction profile across the CL is uniform, and if $\upsilon < 1$, the reaction profile is not uniform and the utilization of the catalyst is not 100%. According to Eq. 25, the penetration depth depends on the loading. At high loadings, the penetration depth approaches to 0, and thus the utilization is not 100%. At low loadings, however, ε become higher than 1, and consequently the reaction profile is uniform, resulting in the utilization of 100%. The main parameter that influences the penetration depth is the product of $ECSA_{\text{RDE}}\nu_{\text{MEA}}i_0$. If this parameter *i*s high, the reaction is facile, and the penetration depth may be smaller than 1. However, in this case, the reaction is sluggish, and the penetration depth is more likely to be higher than 1. Equation 18 was solved under two different assumptions: (i) the exchange current density is high with facile kinetics and $\upsilon \ll 1$; and (ii) it is small with sluggish kinetics and $\upsilon \gg 1$. The first case is mainly the characteristics of the anode, but as the catalyst activity increases, because of the advanced catalyst,[11,33] it may be of importance with regards to the cathode.

High exchange current density.—When the reaction is facile, a linear kinetics can be applied,[110] which is acceptable for the calculation of the small current region. If the overpotential is less than 5 mV, Eq. 18 can be rewritten to a dimensionless form:

$$\upsilon^2\frac{d^2\hat{j}}{d\hat{x}^2} = \hat{j} \quad [26]$$

where $\hat{j}$ is the dimensionless current density in the electrolyte and $\hat{x}$ is the dimensionless length of the CL. Assuming $\upsilon \ll 1$, we reach the following expression for the current–potential relationship:

$$i = \sqrt{\frac{2\alpha nF\cdot\sigma_{\text{Nafion}}a_{\text{Pt}}i_0}{RT}}\eta \quad (\upsilon \ll 1) \quad [27]$$

Under these assumptions and typical loadings (0.1–0.4 mg cm^{-2}), the current does not depend on the loading because the penetration depth is much smaller than the electrode thickness. MA can be formulated by substituting the current with the mass specific current and Eqs. 8, and 21:

$$i_{\text{m}} = \frac{1}{m_{\text{Pt}}}\sqrt{\frac{2\alpha nF\cdot ECSA_{\text{RDE}}\nu_{\text{MEA}}i_0(1-\varepsilon_{\text{V}})}{RT\cdot Y_0}}\cdot\eta \quad [28]$$

Therefore, MA is inversely proportional to the loading. For SA, we reach

$$i_{\text{Pt}} = \frac{1}{m_{\text{Pt}}}\frac{1}{\sqrt{ECSA_{\text{RDE}}\nu_{\text{MEA}}}}\sqrt{\frac{2\alpha nF\cdot i_0(1-\varepsilon_{\text{V}})}{RT\cdot Y_0}}\cdot\eta \quad [29]$$

In the case of highly active catalyst, MA and SA are not a good measure of the catalytic activity. Both parameters depend on the mass loading and the ECSA because of the variation of utilization caused by a non-uniform reaction profile through the cross-section of the CL even at 0.9 $V_{iR\text{-corrected}}$.

Small exchange current density.—The charge-transfer reaction was considered to follow the Erdey-Grúz-Volmer kinetics[111]:

$$S(\eta) = I_{\text{anodic}}(\eta) - I_{\text{cathodic}}(-\eta) \quad [30]$$

where the anodic and cathodic parts are assumed to be symmetrical. This may not fully correct because the ORR is a highly irreversible reaction. However, in our modeling domain, the Tafel approximation may give higher inaccuracy. If one considers the diffusion limiting current through the covering Nafion® film (I_{film}) and the effectiveness factor of the agglomerate, we reach

$$\frac{1}{I_{\text{cathodic}}} = \frac{1}{I_{\text{film}}} + \frac{1}{I_{\text{kinetic}}} \quad [31]$$

$$I_{\text{kinetic}} = \frac{Eff}{nFc_{\text{ref}}}\exp\left(-\frac{\alpha F}{RT}\eta\right) \quad [32]$$

where *Eff* is the effectiveness factor taken from the literature.[93] I_{anodic} was determined by the same method as Eqs. 31 and 32. The number of electrons involved is considered as 1. The polarization curves and the MA were simulated by using Matlab ODE solver. The values of the parameters were used from Ref. 91 and the measured values from Tables I and II.

The variation of the physical properties of the CL in Table II indicates that the increase of the loading affected the pore structure

of the CL. Three main effects were found: (i) increase of the agglomerate's radius; (ii) increase of the pore diameter and the simultaneous slight increase of the porosity; and (iii) decrease of the fractal dimension. During the simulation, the porosity was varied from 10% to 80%, the ECSA from 20 to 140 $m^2\ g^{-1}$, the agglomerate size from 10 to 200 nm, and the Nafion® film thickness from 1 to 5 nm. In every cycle, the Pt loading was varied from 0.05 to 0.5 mg cm^{-2} so finally every combination of the parameters was compared.

Figure 4 shows the SA as a result of the consecutive runs.[102] Generally, it was found that the oxygen concentration was uniform in the gas pores and the effectiveness factor was close to 1 at 0.9 $V_{iR\text{-corrected}}$. The variation of ECSA has no effect, and the agglomerate size and the Nafion® film thickness have a weak effect on the variation of MA and SA. The SA as a function of loading and porosity is shown in Fig. 4a, which indicates that as the loading and the porosity increase, the SA decreases. However, the decrease was only 12%, which was much smaller than the decrease found in the experiments in Table I. Figure 4a also shows that the SA is independent of the catalyst loading over a very broad range. Figure 4b shows the effect of the agglomerate size—the trend is the same, but the decrease of SA is smaller than in Fig. 4a, which reflects the slight decrease of the effectiveness factor. Figure 5a shows the effect of Pt loading on the polarization curves in Tafel representation.[102] The modeled polarization curves have the same trend as the measured ones, i.e., the current density decreases with a decrease in loading. Figure 5b shows the calculated Pt specific currents.[102] When the Pt loading increased, the SA decreased as it was found in the experiments in Table I, although there are some important differences observed. First, the proportion of the decrease was much smaller than it was observed in the experiments. Second, as the Pt loading increased, the Tafel slope increased. In contrast, we found the same Tafel slopes at all loadings in Table I. The increase of the modeled Tafel slope is the consequence of earlier appearance of the transition state because of the poorer proton transport in the thicker and more porous CL. Consequently, the MA was influenced by other parameters of the structure because the validity of the kinetic region loses its validity. However, there always exist a broad range of parameters where the kinetic asymptotic solution is valid, i.e., the MA and SA may be independent of the loading. It has been reported in the literature that the MA increases as the loading decreases.[50,60,76–79,81] It was concluded that the better access of O_2 to the catalyst sites is the reason for the enhanced MA because of the higher porosity of the thinner CL. The result suggests that the increase in porosity decreases the MA, especially at very high porosities (80%–90%). The observed Tafel slopes were higher (–88 mV dec^{-1}) than the theoretically expected values (–70 mV dec^{-1}). These observations indicate that the decrease of the MA is likely the effect of loss of validity of the Tafel approximation.

Non-linear scaling.—An attempt was made to consider the variation of the structure of the CL by incorporating the fractal dimension into the spherical agglomerate model. The model assumes that the CL is built up by spheres of similar dimension taping each other (no overlapping). In this case, the volume $V(r)$ of the CL can be filled up by agglomerates with a radius r and a volume $4/3\pi r^3$, respectively. This requires $N(r)$ spheres to fill out the entire volume, according to the following relationship:

$$V(r) = N(r) \cdot \frac{4}{3}\pi r^3 \qquad [33]$$

hence, the density of the spheres/agglomerates is proportional to r^{-3}. In reality, it is very difficult to determine where the agglomerates start and end, because of their self-assembling nature and the very different size of the agglomerates' building blocks, the carbon. If smaller and smaller spheres are used as a yardstick, i.e., r approaches zero, the volume and the density converge to the real value; however, in this case, Eq. 33 is not generally valid. If the object has any self-similarity, the density of the agglomerates is proportional to r^{-D_f} where D_f is smaller than the embedded Euclidean dimension (i.e., 3). The non-linear scaling factor (P_{MEA}) can be approximated as the ratio of the real agglomerate density and the (theoretical) density predicted by the spherical agglomerate model:

$$P_{MEA} = \frac{\rho_{Pt}^{real}(D_f)}{\rho_{Pt}} \approx r^{3-D_f} \qquad [34]$$

P_{MEA}, therefore, depends on the fractal dimension exponentially. If $D_f = 3$, i.e., spherical particles fill out the volume with the identical size (according to the spherical agglomerate model), $P_{MEA} = 1$; otherwise, its value is between 1 and $r \ll 1$ (but not zero). Figure 6a depicts the dependency of the non-linear scaling factor on the fractal dimension and on the loading, while Fig. 6b shows that the fractal dimension linearly depends on the loading in Table II.[102] If the nonlinear scaling factor decreases, then the agglomerate density decreases.

The experimental data in Table I shows an exponential decay in the SA, which agrees with Eq. 34. Accordingly, the SA decrease is the consequence of the decrease in the fractal dimension measured, which decreases the non-linear scaling factor and hence decreases

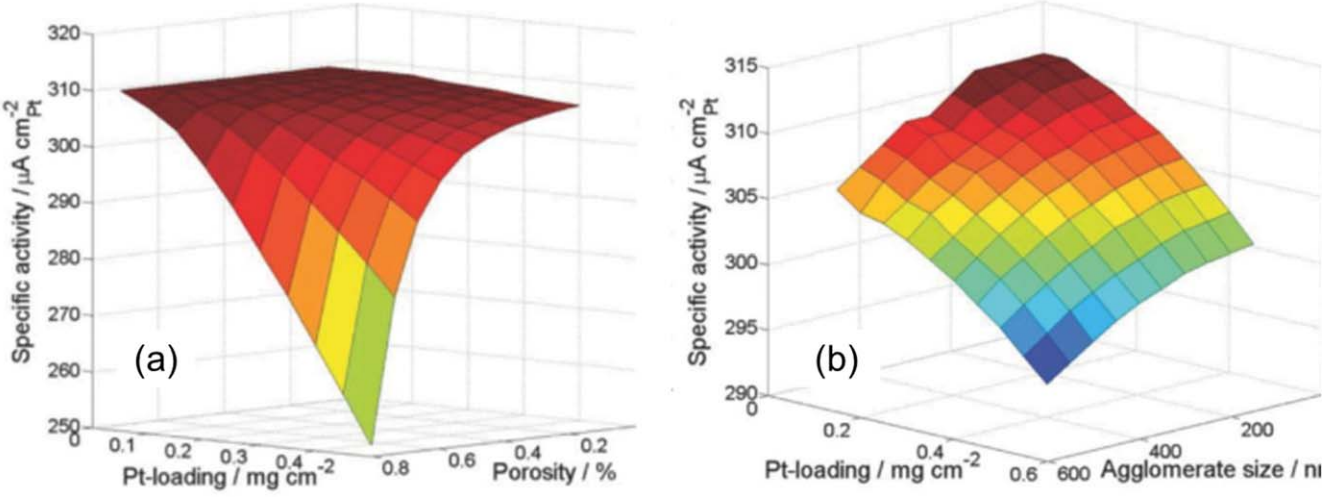

Figure 4. (a) Calculated SA at different loadings and porosities and 50 nm constant agglomerate size, and (b) at different agglomerate sizes and 54% porosity. The plots were calculated using the spherical agglomerate model at 0.9 $V_{iR\text{-corrected}}$. Reprint from permission from Ref. 102; Copyright 2013, Electrochemical Society.

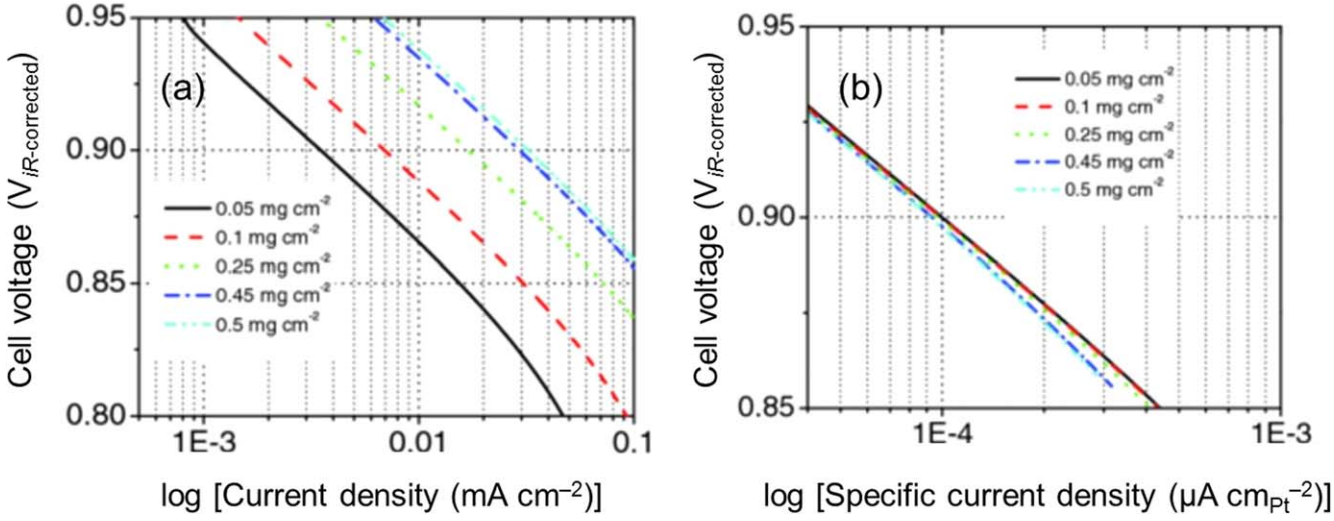

Figure 5. (a) Calculated current densities and (b) specific current densities at different catalyst loadings and 73% porosity in Tafel representation. The plots were calculated according to the uncorrected spherical agglomeration model. Reprint from permission from Ref. 102; Copyright 2013, Electrochemical Society.

the active surface area of the catalyst per unit volume. Equation 34 can be rewritten as:

$$r^{3-D_f} = \exp\left[\log r \cdot (3 - D_f)\right] \quad [35]$$

therefore, the proportionality factors of the non-linear scaling factor can be estimated by using the following semi-empirical function:

$$P_P = y_0 + A \exp\left[B(3 - D_f)\right] \quad [36]$$

where A, B, and y_0 are the proportionality factors. Equation 36 was incorporated into the spherical agglomerate model (Eq. 9) and simulated until a reasonable fit was obtained. Figures 7 and 8 show the results of the numerical model with the fitted values of Eq. 36 ($A = 1.521$, $B = -20.48$, and $y_0 = 0.64$).[95] Figure 7 compares the polarization data measured and simulated by using the fractal dimension-based non-linear scaling factor. Figures 8a and 8b show the measured and simulated mass specific current and MA, respectively. The modified model reflects the experimentally found phenomena, i.e.; when the loading decreased, the geometric current density decreased, and the MA and SA increased. The porosity, agglomerate size, and Nafion® film thickness affect the Tafel approximation in the kinetic region and consequently the measurement of MA and SA. If the nature of the contact between the particles varies, which can be described by the fractal dimension, the active area of the catalyst per unit volume varies. The variation of porosity and agglomerate size accounts for only 5%–10% variation in MA and SA. The variation of fractal dimension, i.e., shape, size, and overlapping of the particles, causes much higher alteration in MA and SA, but it does not affect the validity of the Tafel approximation, because the Tafel slope is unchanged, as shown in Fig. 7.

The impact of Pt/C loading on the MA and mass transport losses of PEMFCs was investigated using experimental and simulation techniques.[63] The results indicated that, as the Pt loading decreased from 0.4 to 0.05 mg cm^{-2}, the MA increased by a factor of 2.7, but at the same time, the mass transport resistance increased. To explain the observed phenomena, a novel CL model was suggested based on a self-assembled, self-similar structure rather than randomly distributed spherical agglomerates. The utilized volumetric surface area, the diffusion through the covering Nafion® film, the Thiele

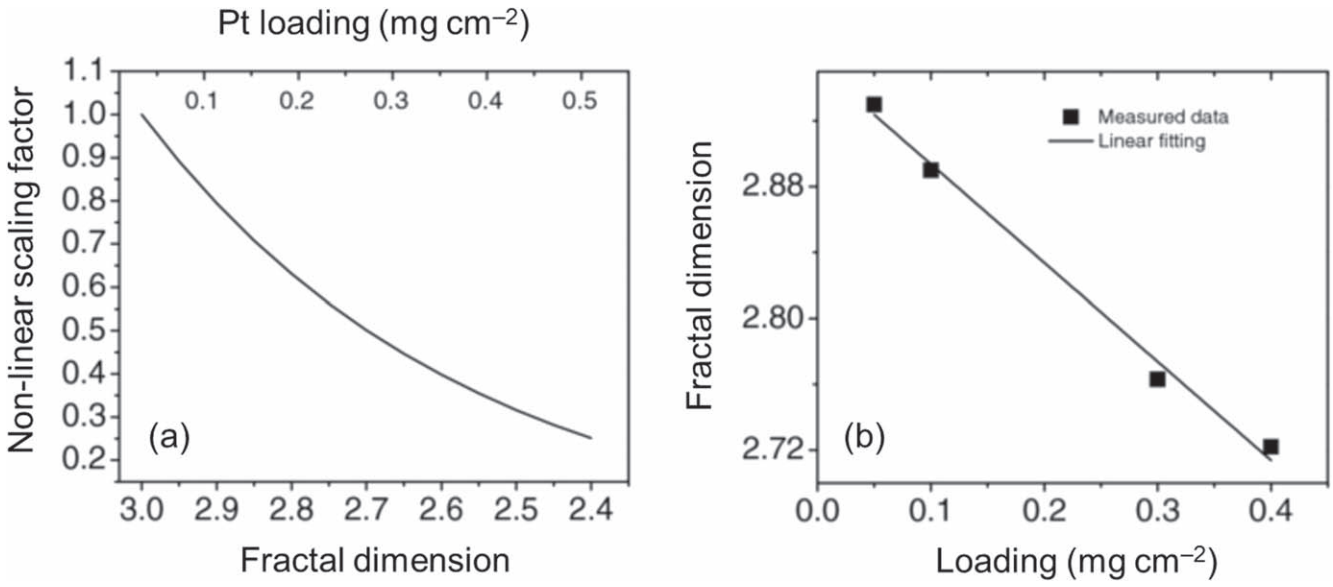

Figure 6. (a) Theoretical variation of the non-linear-scaling factor vs the fractal dimensions and (b) the measured fractal dimensions vs loading. Reprint from permission from Ref. 102; Copyright 2013, Electrochemical Society.

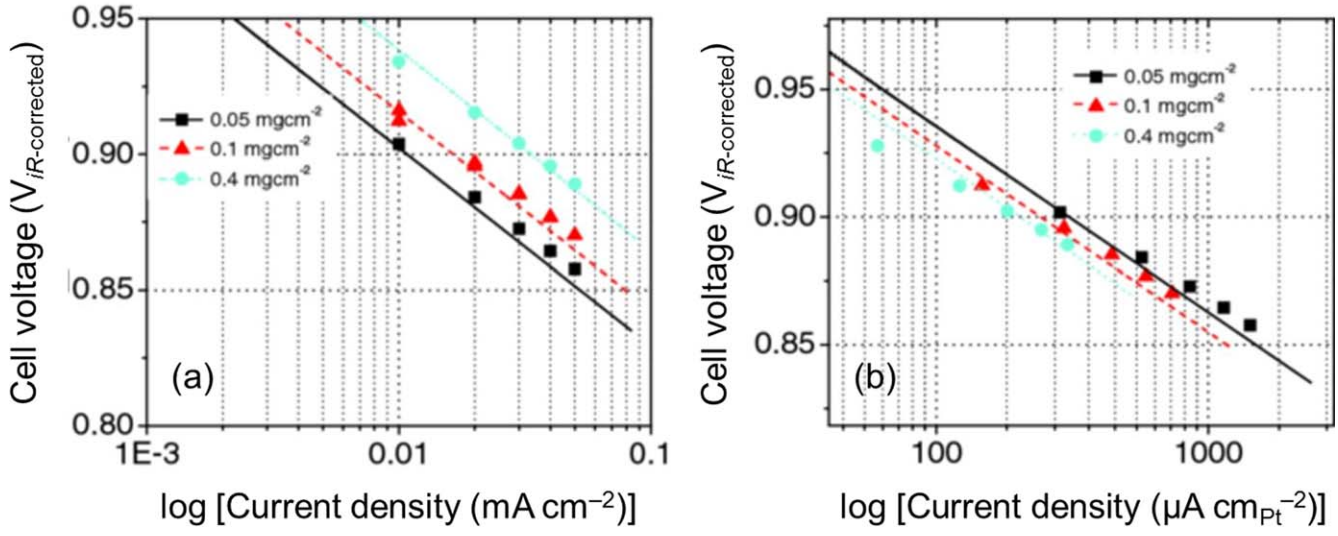

Figure 7. (a) Polarization curves and (b) Pt specific currents measured (scatter) and simulated (line) using the fractal dimension-based non-linear scaling factor. Reprint from permission from Ref. 102; Copyright 2013, Electrochemical Society.

modulus, and the gas phase diffusion were estimated using a fitting algorithm. The self-assembled nature of the CL was supposed to be characterized by its fractal dimension. It was measured independently by Hg porosimetry and found to increase from 2.7 to 2.93 as the Pt loading decreased from 0.4 to 0.05 mg cm^{-2}. The fractal dimension has been incorporated into the macro-homogeneous model, which resulted in the observed increase of mass activity. Correlation is proposed between the fractal dimension and Thiele modulus, which accounts for the simultaneous deterioration.

Development of Highly Active and Durable Hybrid Compressive Pt Lattice Catalysts with Ultra-low Pt Loadings for PEMFCs

The objective was to develop unique hybrid cathode catalysts through interaction of highly active and stable compressive Pt lattice (Pt*) catalysts[51,52,65,112,113] with catalytically active carbon composite support.[50,54–58,63,88,112,113] The goal was (i) to enhance the activity by increasing the synergistic effect of the catalytic sites present in ACCS and those in Pt*[52,58,65,88,112,113]; (ii) to identify the best Pt–Co composition to accomplish high initial performance and stability; and (iii) to perform electrochemical and durability studies of Pt*/ACCS. Figure 9 illustrates the schematic diagram for the synthesis of ACCS. The ACCS was used to synthesize both Pt/ACCS and Pt*/ACCS catalysts.

Synthesis of activated carbon composite support (ACCS).— Catalytically active and stable ACCS and Pt* were developed with optimized surface area, porosity, pore size, and pore size distribution. The hydrophilic/hydrophobic ratio and structural properties (amorphous/crystalline ratio) were engineered to form active sites on the surface of ACCS through metal-catalyzed pyrolysis.[50,52,65,88,112,113] The ACCS was prepared using the procedure developed at USC.[50,54–56,63] In brief, carbon black (*e.g.*, Ketjen Black EC 300J) was treated with HNO_3 at 80 °C under refluxing conditions, and then $Co(NO_3)_2$ and ethylene diamine, used as Co and N precursors, respectively, were mixed with the oxidized carbon black. The molar ratio of Co and N precursors was maintained at 1:9. The mixture was refluxed at 85 °C, and the powder was subjected to heat-treatment in Ar at 800 °C, followed by leaching in H_2SO_4 to remove excess Co from the carbon surface. The ACCS was synthesized using purification and stabilization procedures to remove the electrochemically unstable amorphous carbon in the support.[50,58,65,112,113]

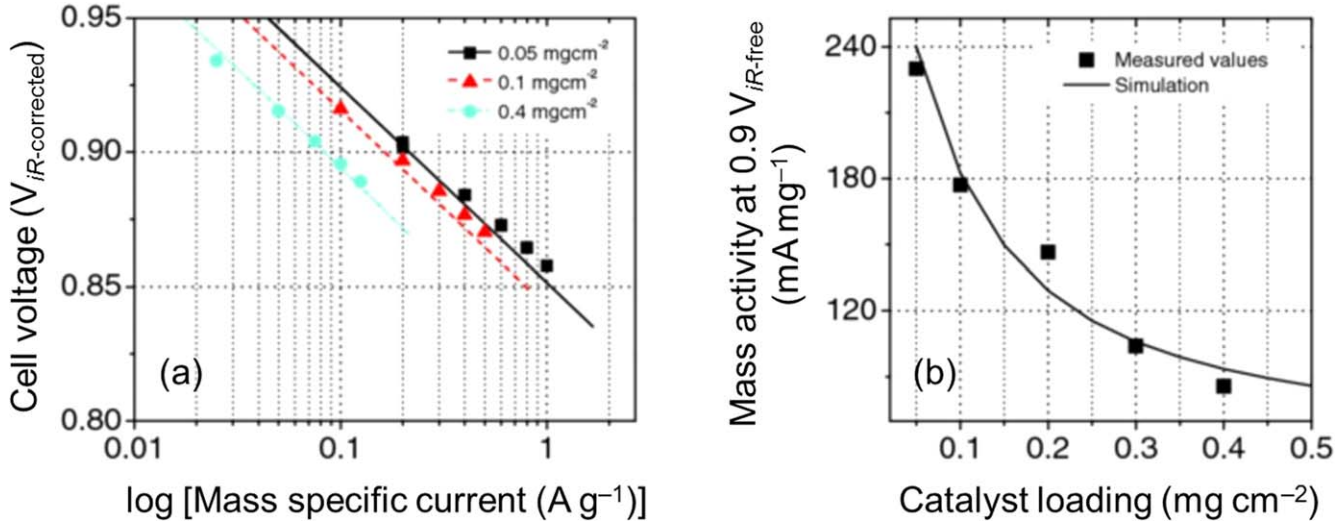

Figure 8. (a) Mass specific current and (b) mass activity measured (scatter) and simulated (line) using the fractal dimension-based non-liner scaling factor. Reprint from permission from Ref. 102; Copyright 2013, Electrochemical Society.

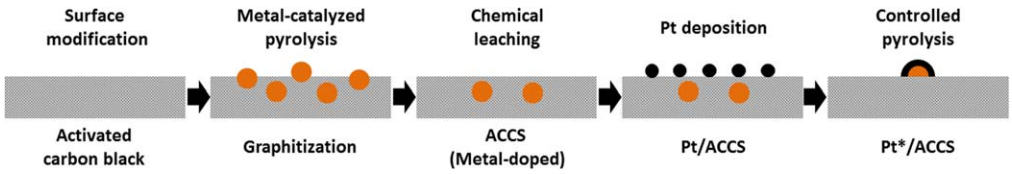

Figure 9. Schematic diagram for the synthesis of Pt/ACCS and Pt*/ACCS catalysts.

Synthesis of Pt/ACCS and Pt*/ACCS.—The following constraints were addressed when developing the hybrid catalyst: (i) accomplish chemical and electrochemical stability of the catalyst and the support at high potentials, low pH, and high temperatures; (ii) design an ACCS with an onset potential and kinetic activity similar to those of Pt; and (iii) develop highly active and stable Pt shell–Co core catalysts. A surface functionalization process was developed to increase the hydrophilic property of ACCS by interacting pyrenecarboxylic acid (a bifunctional organic molecule that contains aromatic hydrocarbon and acid groups) with ACCS.[50,58,65,112,112] The surface modification process is a necessary step in the catalyst synthesis, since it controls both the particle size and distribution of Pt over the support surface.

The Pt/ACCS was synthesized using a modified polyol method.[52,65,112,113] $PtCl_4$ was dissolved in ethylene glycol, followed by the addition of support (ACCS or carbon black) in the solution. NaOH was used to adjust the pH of the solution to 12. Next, the solution was refluxed at 160 °C in an inert atmosphere, followed by cleaning and drying under vacuum. The Pt*/ACCS was synthesized by annealing the Pt/ACCS sample with polyaniline as the protective coating. The USC-developed process yields uniform particle size distribution (3–4 nm). Oxidative polymerization of aniline sulfate was performed at room temperature using ammonium peroxysulfate as the oxidizing agent.[52] The polyaniline-coated Pt/ACCS was then subjected to heat-treatment under reducing atmosphere. Monolayers of Pt* (core/shell Pt_3Co_1) were structured by diffusing Co atoms (present in the support) into Pt. During the controlled heating process, Co diffuses to the surface and forms Pt*/ACCS.

Carbon support characterization and support stability test.—Improved activity and stability of Pt*/ACCS are due to the synergistic effect of catalytic activity and stability of ACCS and the formation of compressive Pt* lattice. To examine the electrochemical stability of carbon support material under PEMFC conditions, various methods have been suggested.[114] Generally, it is required to operate more than 5,000 h to apply PEMFC to the automotive application.[13] However, it is impractical and inefficient to estimate the stability under practical conditions because of long testing time and high cost. The U.S. Department of Energy (DOE), U.S. Fuel Cell Council (USFCC), and the Fuel Cell Commercialization Conference of Japan (FCCJ) proposed several effective AST methods to test the stability of catalysts.[115–118] A good AST method should meet several conditions: (i) relatively short testing time; (ii) good selectivity of carbon degradation; and (iii) good degradation behavior of fuel cell performance.[119]

To establish appropriate AST protocols to meet all the conditions mentioned above, it is important to understand the mechanism of carbon corrosion at various potential regions and potential profiles (constant potential, triangular cycling, rectangular cycling, etc). Reiser et al. suggested that a cathode interfacial potential difference would be increased up to ~1.5 V due to the "H_2/air front" mechanism in the case of start-up/shut-down process.[120] The same phenomenon also occurs in the case of local hydrogen starvation in the MEA.[121] It has been shown that the cathode potential behavior follows a triangular change with the maximum potential of ~1.5 V when H_2 was introduced to the anode compartment.[118] Hashimasa et al. studied the effects of the potential waveform on the carbon corrosion rate by comparing 1.3 V constant potential and 0.9–1.3 V potential cycling for carbon support stability.[119] If the carbon corrosion is only affected by high potential, holding the potential at high value would show a high carbon corrosion rate. However, the carbon corrosion rate for 0.9–1.3 V potential cycling was higher than that for 1.3 V constant potential. Park et al. proposed the reason for this phenomenon as follows: the de-passivated Pt at the lower potential catalyzes carbon corrosion when the potential is increased.[122] The result shows that the potential cycling is more effective than the potential holding to test carbon corrosion. But there is still an issue about the lower potential limit of potential cycling; potentials lower than 0.9 V in the potential cycling would also result in Pt degradation through the Pt oxidation and reduction processes.[123] Therefore, the performance loss by carbon corrosion and the one by Pt degradation would be mixed, resulting in the poor selectivity of carbon support degradation. Thus, the potential above 1.0 V at which Pt is passivated all the time should be used as the lower potential limit of a potential cycling test to study the carbon support stability without the contribution of Pt degradation.

According to all these studies, the potential cycling between 1.0 and 1.5 V would be a good AST protocol to test the carbon support stability in PEMFCs. Actually, the FCCJ suggested a potential cycling protocol (1.0–1.5 V, 5,000 cycles, and 500 mV s^{-1}) to test the support stability in 2011,[118] and the DOE revised their previous protocol (1.2 V constant potential for 400 h) with the same protocol as the FCCJ in 2013.[124] This protocol also reduces the testing time (2 s per cycle, < 3 h total). Mukundan reported the comparison of the old protocol (1.2 V constant potential) and the new protocol (1.0–1.5 V cycling) of the DOE.[125] It was observed that 200 h constant potential at 1.2 V is equivalent to 2,000 cycles at 1.0–1.5 V. According to the result, the author concluded that the new protocol could reduce the testing time significantly (~100 times) when compared to the old protocol with the same performance decay. Due to the advantages mentioned above, in this review, the 1.0–1.5 V potential cycling protocol has been presented for the stability test of carbon supports for Pt or Pt alloy catalysts.

The crystallite thickness (L_c) calculated by Scherer's formula and the interlayer spacing (d_{002}) obtained from Bragg's law were used as the factors to determine the degree of graphitization of the carbons. Higher L_c value of the (002) peak and lower d_{002} number imply a higher degree of graphitization.[53,58,59,61,65,88,112,113,126] The ACCS showed L_c value that was almost twice higher than that of Ketjen Black and the lowest d_{002} of 0.349 nm when compared to Ketjen Black and Ensaco 290G. The X-ray diffraction (XRD) analysis indicated that the higher degree of graphitization observed for ACCS when compared with the Ketjen Black can be attributed to the higher thermal stability of ACCS. The hydrophilic/hydrophonbic properties of ACCS were tested by despersing the carbon supports in a water/hexane mixture. The ACCS showed dispersion mainly in the hexane phase attributted to the higher degree of its hydrophobic caracter when comapred with Ketjen Black. The enhanced hydrophobic property of ACCS was also confirmed by the contact angle measurements. The contact angle of 132° estimated for ACCS was much greater than that for Ketjen Black (38°), indicating enhanced hydrophobicity. The enhanced hydrohobic property of ACCS minimizes water adsorption, resulting in less carbon corrosion and, as will be shown later, which increases PEMFC performances in the mass transport region. The functionalized ACCS support maintains stable dispersion during Pt deposition in aqueous media. The USC-developed activation process uses organic molecules containig hydocarbon and acid groups. The stability was attributed to the

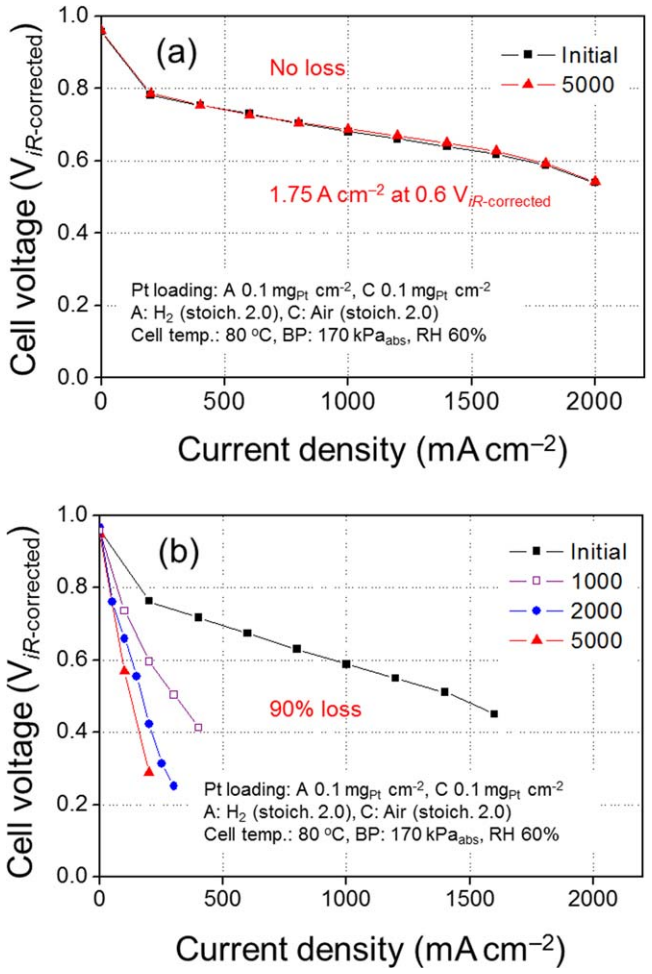

Figure 10. Support stability of (a) 30 wt% Pt/ACCS and (b) commercial Pt/C under 1.0–1.5 potential cycling for 5,000 cycles. Reprint from permission from Ref. 50; Copyright 2016, Elsevier.

grafting of functional groups with negative charges, which provides electrostatic stability required for colloidal dispersion.[56,57] After Pt deposition, the functional groups were removed from carbon surface. The support stability tests were carried out by subjecting the MEAs to a potential cycling test (1.0–1.5 V, 5,000 cycles) to simulate the start-up/shut-down conditions of an automotive PEMFC. Oxidation of the carbon surface increases its hydrophilicity and affects water removal, resulting in an increased mass-transfer resistance. In addition, oxidation of carbon increases the electrical resistance of the catalysts, which leads to the detachment or aggregation of catalyst particles and damages the cathode CL structure.

Figures 10a and 10b show H_2/air fuel cell polarization curves for 30 wt% Pt/ACCS and 30% commercial Pt/C (TKK) catalysts, respectively.[50] As shown in Fig. 10a, after 5,000 cycles, the Pt/ACCS showed no performance loss, indicating excellent support stability. On the other hand, commercial Pt/C catalyst showed 90% performance loss after 5,000 cycles. The higher performance of Pt/ACCS is due to optimized support properties: (i) surface area, which resulted in a thin CL, thus favoring effective mass-transfer to the Pt catalytic sites; and (ii) hydrophobicity of ACCS, which resulted in better water removal during high current operations. The results also indicated that Pt/ACCS with the ultra-low Pt loading at operating conditions exhibited excellent support stability due to: (i) synergistic effect through combined activity of the catalytic sites present on ACCS and Pt[50,53,59,61,126]; (ii) well distributed catalyst nanoparticles; and (iii) increased metallic Pt^0 surface concentration due to the fact that the pyridinic-N present in the support played a role of oxide-cleanser.[52,54–57,59] The MAs under H_2/O_2 operating conditions at 0.9 $V_{iR\text{-corrected}}$ were measured before and after the support stability test to examine the kinetic performance changes of the catalysts (Fig. 11).[50] The Pt/ACCS catalyst showed no loss of MA after the support stability test, while commercial Pt/C showed 57.5% loss.[58,59,65,88,112,113]

Performance of ultra-low hybrid catalysts for PEMFCs.— *Effect of protective coating.*—Strasser et al. used a voltammetric dealloying method which uses different redox potentials of metals to prepare a surface with Pt-rich alloys.[27,127] Partial selective elimination of a more reactive metal from a Pt-based alloy was performed by electrochemical dissolution. A reaction-driven method was reported by Tao et al. in which the structure and composition of the core-shell were controlled by the reducing and oxidizing power of the environments.[128] A colloidal method was suggested to prepare noble metal cores in the presence of a capping agent. Next, the metal shell was deposited.[129–131]

Kim et al. developed a novel route based on thermal treatment to synthesize a carbon-supported 5 nm nanoparticles of Pt_2Ni_1 with a Pt-rich shell.[132] A polypyrrole (PPy) layer with a thickness of 3–5 nm encapsulated the surface of previously deposited Pt on carbon support. The organic coating served as a sponge to adsorb the Ni precursor as well as a physical barrier to inhibit the increase in particle size of Pt during the thermal treatment. The PPy layer doesn't act as poison to the core-shell catalyst because it completely decomposes during the heating at high temperatures in a H_2–Ar mixture. By controlling the catalyst particle size during formation of the core-shell Pt_2Ni_1/C at high temperatures, one enhances the catalytic activity of the alloy for ORR when compared to pure Pt/C catalyst. The other benefit of this method is that the PPy protective coating can be easily modified for the synthesis of various carbon-supported core-shell-like catalysts when using heat-treatment to control the severe agglomeration of the catalyst particles.

Pt^*/ACCS was prepared using a methodology developed at USC.[52,65,112,113] Co was used as a doping material to have different atomic ratios of Pt:Co in Pt^*/ACCS. After annealing Co-doped Pt/ACCS at 800 °C in absence of protective coating, the peak position (2θ) for Pt increased from 39.81° to 40.92°, indicating a formation of compressive Pt lattice. However, the particle size of the annealed sample increased to ~6.7 nm from the initial diameter of ~2.9 nm of Pt/ACCS catalyst estimated before the heat-treatment. The large Pt particle size results in small ECSA and poor fuel cell performance. When the annealing was carried out in presence of protective coating, the estimated particle size was ~3.2 nm, while the peak position shifted to 40.92°. The pristine Pt/ACCS showed uniform Pt dispersion.[52,53,59,61,126] Without the protective coating, large particles were seen in the range between 8 and 20 nm.

Effect of annealing temperature.—The effect of annealing temperature on the particle sizes of Pt^*/ACCS was studied in the temperature range between 300 and 900 °C. The corresponding XRD patterns are shown in Fig. 12.[52] The Pt (111) peak was shifted to higher 2θ values as the annealing temperature was increased. Co present in ACCS diffuses to the catalyst surface, forming Co-doped Pt lattice, which was confirmed by the Pt peak shift. The XRD study indicated the presence of Pt and PtCo phases after heat-treatment at 800 °C. Above 800 °C, 2θ values of the Pt (111) peak were stabilized, which indicates a completion of Pt^* formation. The peak shift linearly increased up to approximately 700 °C and remained almost unchanged above 800 °C. The physical and electrochemical properties for Pt/ACCS and Pt^*/ACCS are summarized in Table III. Deconvolution analysis of Pt (111) peaks at 800 °C indicated that choosing the annealing temperature in the range between 700 and 800 °C to synthesize Pt^*/ACCS will maximize the Pt^* formation while maintaining smaller particle sizes of Pt. The formation of the Pt shell–Co core structure on the Pt^* catalyst is shown in Fig. 13. line scanning compositional analysis confirmed the existence of Co within the core of the catalyst particle and Pt shell thickness of 0.5–0.8 nm.

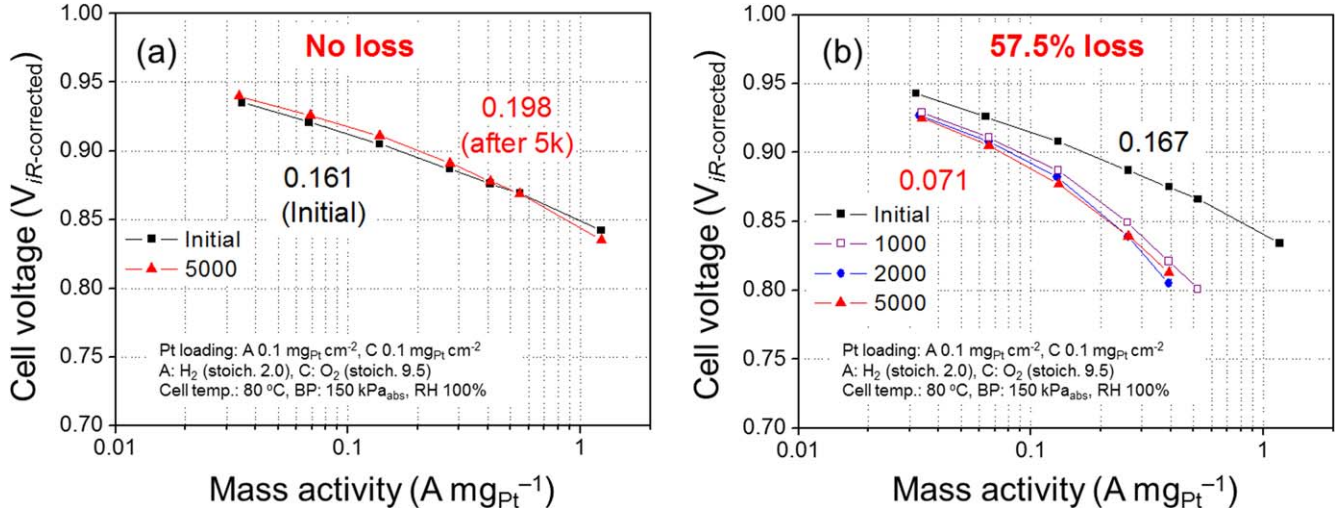

Figure 11. Catalyst stability for (a) 30 wt% Pt/ACCS and (b) 30 wt% commercial (TKK) catalysts under 1.0–1.5 V cycling. Reprint from permission from Ref. 50; Copyright 2016, Elsevier.

Figure 14a compares the cyclic voltammograms of MEAs with Pt/ACCS and Pt*/ACCS.[52] While the ECSA of Pt/ACCS showed a value of 41.0 $m^2\ g_{Pt}^{-1}$ (Table III), the Pt*/ACCS catalysts showed ECSAs lower than 35 $m^2\ g_{Pt}^{-1}$ due to their relatively larger particles sizes than those observed for Pt/ACCS. As the annealing temperature increased, the Pt particle size increased, resulting in a decrease of ECSA. Besides, the Pt* catalyst has altered electronic structure, which lowers the bonding energy between Pt and adsorbates, such as hydrogen. Therefore, the smaller peaks for hydrogen adsorption/desorption were observed, contributing to smaller ECSA (Table III). The MAs of Pt/ACCS and Pt*/ACCS at 0.9 $V_{iR\text{-corrected}}$ under H_2/O_2 condition are shown in Figure 14b[52] and Table III. The MAs of Pt*/ACCS showed more than two times higher values (> 400 mA mg_{Pt}^{-1}) than that of Pt/ACCS (193 mA mg_{Pt}^{-1}). The MA gradually increased to 492 mA mg_{Pt}^{-1} at 700 °C. The observed increase in MA can be attributed to an increase of Pt* formation as a function of the annealing temperature (due to the formation of Pt shell–Co core structures). At 900 °C, a decrease of MA was observed because of the agglomeration of Pt particles.

The H_2/air fuel cell performance was investigated to evaluate the performance of Pt/ACCS and Pt*/ACCS under automotive operating conditions (Fig. 14c).[52] Initially when the measurements were performed at 0.7 $V_{iR\text{-corrected}}$ (mixed ohmic and mass-transfer region), the results indicated that Pt*/ACCS showed 100 mA cm^{-2} higher current densities than Pt/ACCS. The current densities of 1,186 mA cm^{-2} and 1,143 mA cm^{-2} (Table III) were observed at 0.7 $V_{iR\text{-corrected}}$ for Pt*/ACCS catalysts annealed at 700 °C and 800 °C, respectively, compared with 1,011 mA cm^{-2} for Pt/ACCS. The H_2/air performance of Pt*/ACCS at the mass-transfer limitation region showed similar performance when compared to Pt/ACCS. The current densities of 1,889 mA cm^{-2} and 1,800 mA cm^{-2} were observed at 0.6 $V_{iR\text{-corrected}}$ for Pt*/ACCS catalysts annealed at 700 and 800 °C, respectively. These performances were similar to those of Pt/ACCS (1,884 mA cm^{-2}). Lower performances than Pt/ACCS catalyst were observed on the catalysts synthesized below 600 °C and over 850 °C. For the catalysts annealed below 600 °C, the low H_2/air performances are due to the residual coating materials on Pt particles that cover the active site of Pt. The poor performance of the catalysts annealed over 850 °C is attributed to the large Pt particle size and agglomerations.

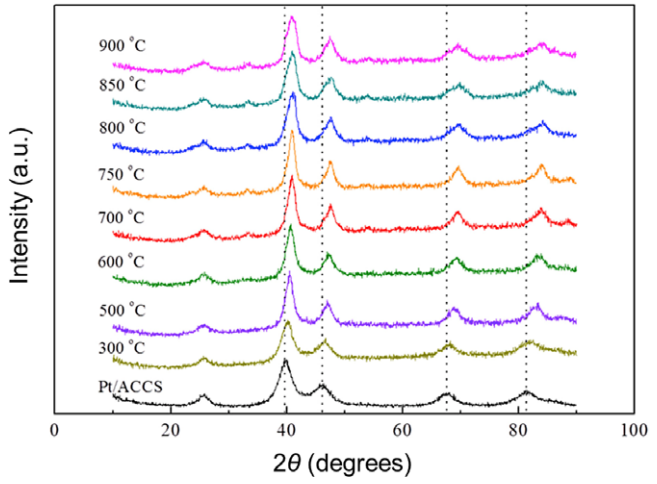

Figure 12. XRD patterns for Pt/ACCS and Pt*/ACCS catalysts synthesized at various temperatures in the range of 300 °C to 900 °C. Reprint from permission from Ref. 52; Copyright 2017, Elsevier.

The reason for the observed phenomenon is the fact that the H_2/air performance is mainly controlled by the kinetic performance of the catalyst at the low current density region but is mostly controlled by the mass-transfer limitation, including O_2 concentration and water removal. Furthermore, for both Pt/ACCS and Pt*/ACCS, only pure Pt would be present on the catalyst surface at 0.6–0.7 V due to the electrochemical reduction of Pt oxides. Thus, the H_2/air performance at low potentials would not be affected as much as in the case of MA measured at 0.9 $V_{iR\text{-corrected}}$. However, the most important achievement of Pt*/ACCS is the improvement of catalyst stability under potential cycling experiments at 0.6–1.0 V. The result of catalyst stability and the mechanism of improvement of catalyst stability will be discussed in the following section.

Effect of Pt:Co ratio.—The Pt/ACCS catalyst possesses high support stability and enhanced catalyst stability when compared to commercial Pt/C catalysts. In order to further improve the catalyst stability, Pt was doped with Co to induce Pt lattice contraction, which decreased Pt* dissolution during potential cycling (0.6–1.0 V). However, doping Pt with excess of Co decreases the ORR activity due to Co coverage on the Pt active sites. On the other hand, our results indicated that a smaller Co content may not be effective to provide the Pt* structure. Therefore, the Pt:Co ratio plays a significant role in catalyst development and needs to be optimized to provide a highly active and stable catalyst.

Various Pt:Co ratios in the range of Pt_4Co_1/ACCS to Pt_1Co_1/ACCS were synthesized using the same Co doping process and annealing conditions (800 °C). The effect of the Pt:Co ratio on

Table III. Summary of the physical and electrochemical properties for Pt/ACCS and Pt*/ACCS catalysts annealed at various temperatures.

Annealing temp. (°C)	d_{Pt} (XRD) (nm)	2θ for Pt (111) (°)	ECSA ($m^2\ g_{Pt}^{-1}$)	MA ($A\ mg_{Pt}^{-1}$)	Current density@ 0.7 $V_{iR\text{-free}}$ ($mA\ cm^{-2}$)	Current density@ 0.6 $V_{iR\text{-free}}$ ($mA\ cm^{-2}$)	Rated power density ($g_{Pt}\ kW^{-1}$)
Pt	2.9	39.81	41.0	0.193	1011	1884	0.174
300	3.0	40.18	-	-	-	-	-
500	4.1	40.50	34.2	0.425	1028	1418	0.229
600	4.1	40.65	30.5	0.458	1018	1395	0.237
700	4.7	40.81	30.4	0.492	1186	1889	0.173
750	4.6	40.86	—	—	—	—	—
800	3.2	40.92	26.1	0.474	1143	1800	0.180
850	3.0	40.90	28.4	0.471	930	1488	0.207
900	2.9	40.89	26.6	0.408	917	1308	0.250

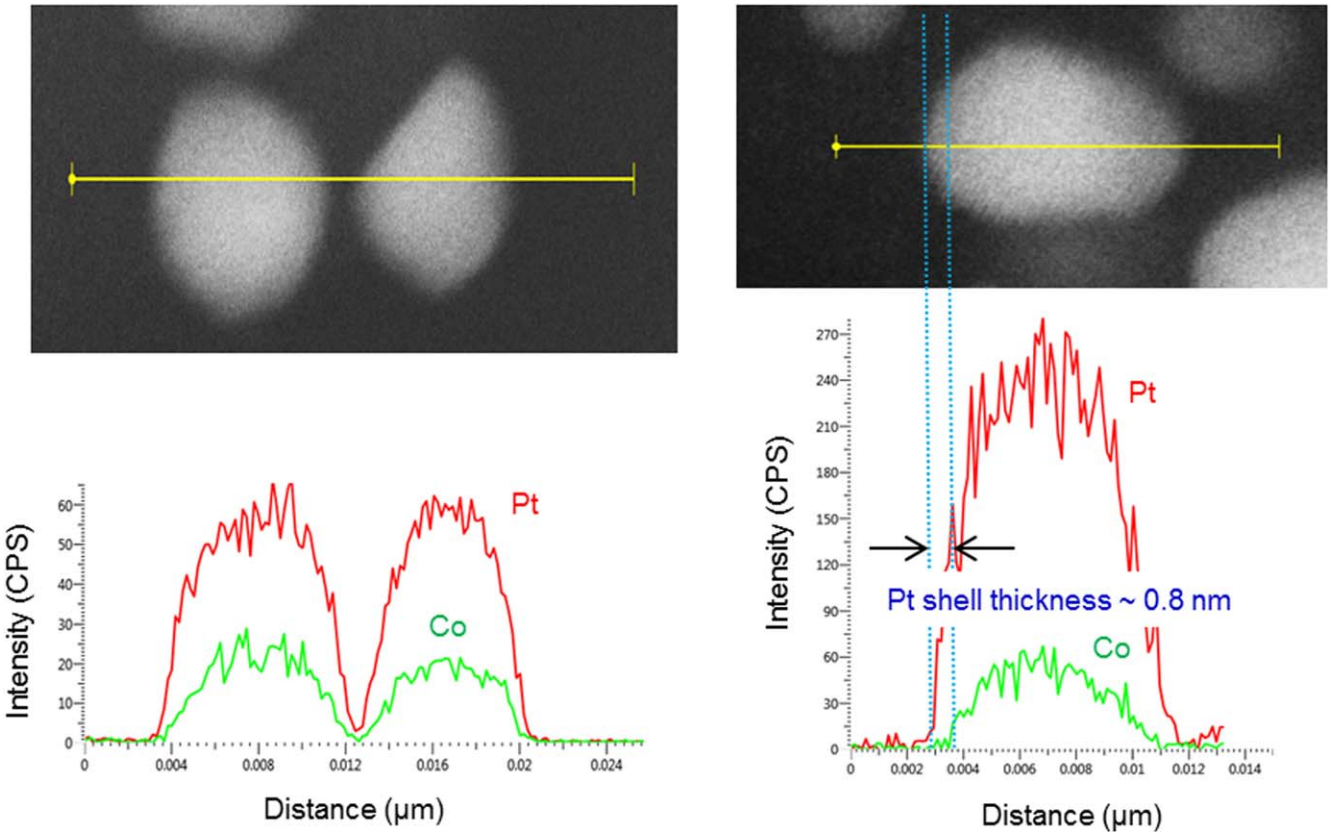

Figure 13. Line scanning compositional analysis for Pt*/ACCS.

the particle size and Pt structure is shown in Fig. 15.[52] All Pt*/ACCS catalysts with various Pt:Co ratios showed peak shifts in the XRD data. The Pt*/ACCS synthesized with a higher amount of Co exhibited a higher shift, indicating that more Pt* sites have been formed during the annealing process. Furthermore, Pt particle sizes of Pt*/ACCS measured by XRD patterns showed the values in the range of 3–4 nm due to the controlled annealing with protective coating.

As shown in Fig. 16a,[52] as the Co amount increased in Pt*/ACCS, the MA increased due to the formation of more Pt* sites. Most of Pt*/ACCS catalysts annealed at various temperatures showed 2θ values for Pt (111) higher than 40.50° and MAs of $>$ 400 mA mg_{Pt}^{-1}. However, Pt_4Co_1/ACCS and Pt_3Co_1/ACCS showed 2θ values of 40.29° and 40.46° and MAs of 329 and 344 mA mg_{Pt}^{-1}, respectively, which are smaller than those of the annealed catalysts (Table IV). These results indicate that the Pt:Co ratio is a more sensitive factor than the annealing temperature to form Pt* catalyst. The H_2/air fuel cell performances for Pt/ACCS and Pt*/ACCS synthesized with various Pt:Co ratios are shown in Fig. 16b.[52] The Pt_2Co_1/ACCS and Pt_3Co_1/ACCS showed similar performances (1,847 mA cm^{-2}) with that of Pt/ACCS. The Pt_1Co_1/ACCS catalyst showed a lower performance (1,230 mA cm^{-2}) due to excess Co, when compared to that of Pt/ACCS (1,884 mA cm^{-2}). Based on the physical and electrochemical properties of various Pt*/ACCS catalysts with different Pt:Co ratios, a catalyst with a composition of Pt_3Co_1/ACCS catalyst annealed at 800 °C was selected and subjected to support stability (1.0–1.5 V) and catalyst stability (0.6–1.0 V) studies under potential cycling conditions.

Support stability test.—Prior to the stability tests, the reproducibility of Pt*/ACCS (i.e., 30 wt% Pt_3Co_1/ACCS) was tested by fabricating five different MEAs and testing their fuel cell performances, as shown in Fig. 17. All four MEAs showed excellent agreement of H_2/air performance and MA results within ±4% difference. The fuel cell performance and MA of Pt*/ACCS subjected to 1.0–1.5 V cycling test is shown in Fig. 18a.[52] The Pt*/ACCS catalyst showed an initial potential of 633 $mV_{iR\text{-corrected}}$ at 1,500 mA cm^{-2} and a potential loss of 8 mV at 1,500 mA cm^{-2} after 5,000 cycles. The commercial Pt/C catalyst showed 481 $mV_{iR\text{-corrected}}$ at 1,500 mA cm^{-2} for initial performance and no activity after 1,000 cycles. The MA of Pt*/ACCS in Fig. 18b showed 341 mA mg_{Pt}^{-1} for initial performance and 50% loss after 5,000 cycles.[52] The commercial Pt/C showed an initial MA of 167 mA mg_{Pt}^{-1} and 80 mA mg_{Pt}^{-1} after 5,000 cycles. The good support stability of Pt*/ACCS is attributed to the stable ACCS support and formation of compressed core-shell Pt lattice.

Table IV. Summary of the physical and electrochemical properties for Pt/ACCS and Pt*/ACCS catalysts synthesized with various Pt/Co ratios.

Catalyst	Annealing condition	2θ for Pt (111) (°)	d_{Pt} (XRD) (nm)	MA (A mg_{Pt}^{-1})	Current density @0.6 $V_{iR\text{-free}}$ (mA cm^{-2})
Pt/ACCS	800 °C 4 h with protective coating	39.87	2.9	0.193	1884
Pt_4Co_1/ACCS		40.29	3.8	0.329	1545
Pt_3Co_1/ACCS		40.46	3.8	0.344	1847
Pt_2Co_1/ACCS		40.92	3.4	0.474	1800
Pt_1Co_1/ACCS		41.48	3.3	0.484	1230

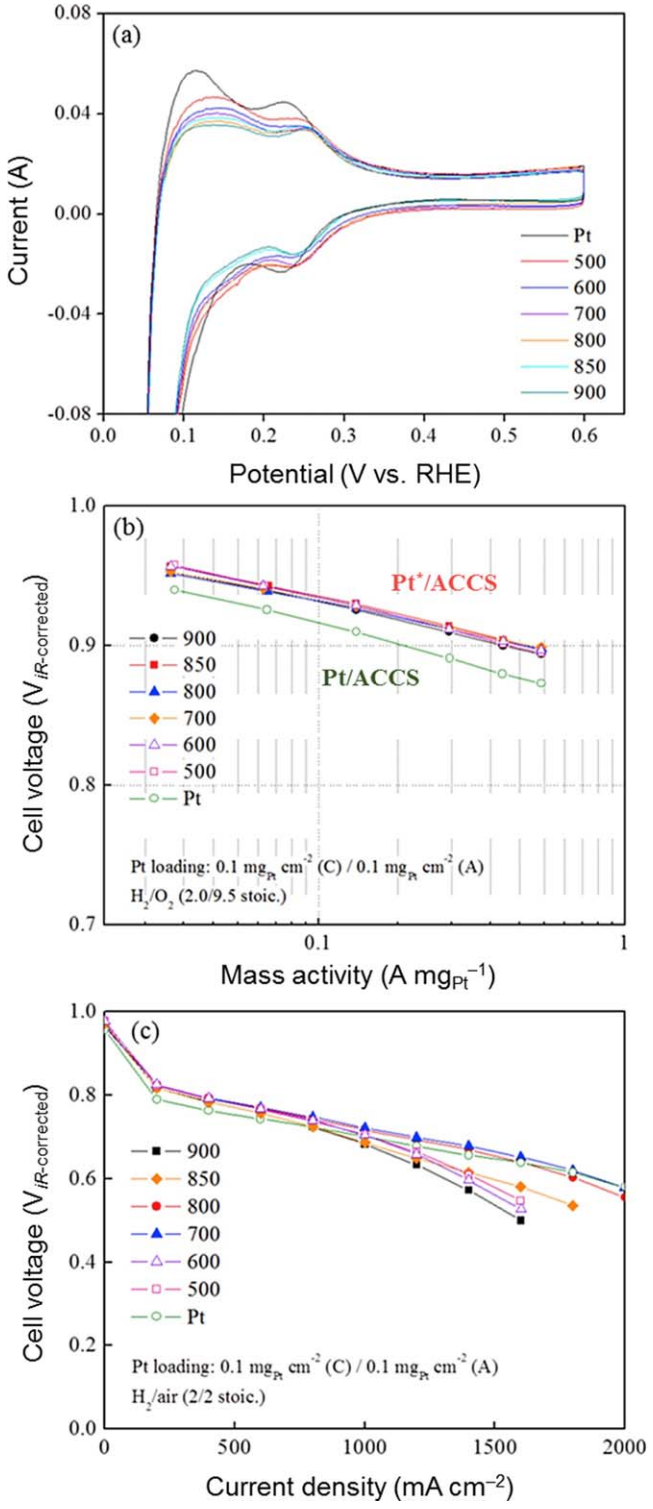

Figure 14. Comparison of (a) cyclic voltammograms, (b) MAs, and (c) H_2/air polarization results in MEAs for Pt/ACCS and Pt*/ACCS. Reprint from permission from Ref. 52; Copyright 2016, Elsevier.

Catalyst stability test.—Figure 19a shows the H_2/air fuel cell performance of Pt*/ACCS tested in 25 cm^2 MEA subjected to 0.6–1.0 V cycling test.[52] Pt*/ACCS showed an initial potential of 729 $mV_{iR\text{-corrected}}$ at 800 mA cm^{-2} with a potential loss of 24 $mV_{iR\text{-corrected}}$ after 30,000 cycles. The commercial Pt/C showed an initial potential of 696 $mV_{iR\text{-corrected}}$ and no activity after 30,000 cycles. MA decreased from 344 to 189 mA mg_{Pt}^{-1} (Fig. 19b).[52]

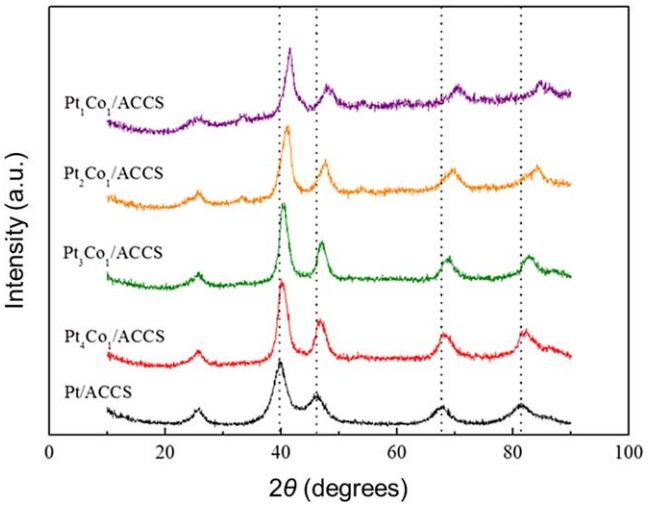

Figure 15. XRD patterns for Pt/ACCS and Pt*/ACCS catalysts synthesized with various Pt:Co ratios. Reprint from permission from Ref. 52; Copyright 2016, Elsevier.

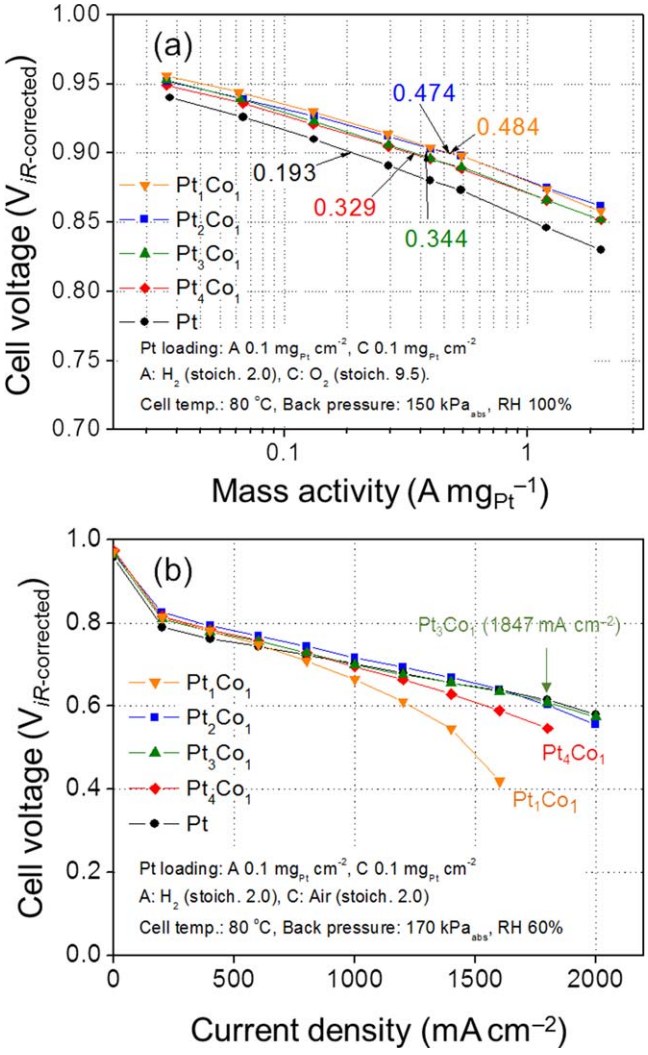

Figure 16. Comparison of (a) MA and (b) H_2/air polarization results for Pt/ACCS and Pt*/ACCS with various Pt:Co ratios. Reprint from permission from Ref. 52; Copyright 2016, Elsevier.

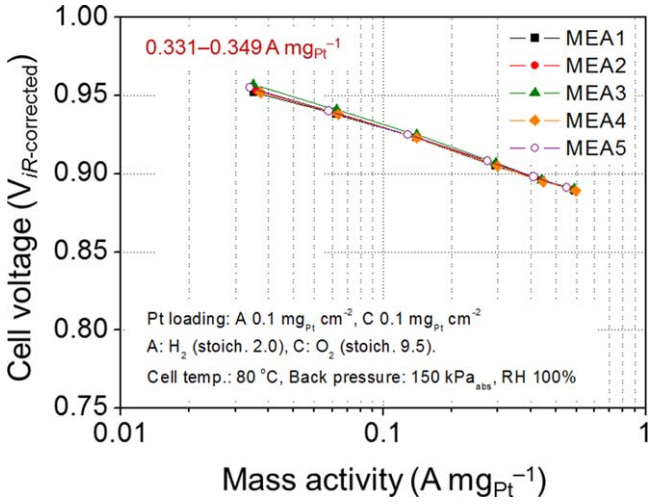

Figure 17. Reproducibility of MA of Pt*/ACCS for five MEAs.

Line scanning analysis before and after the cycling test of 30,000 cycles (0.6–1.0 V) is shown in Fig. 20. The results indicated that the Pt shell thickness increased from 0.7–0.8 nm (2–3 monolayers) to ~2.4 nm (8–10 monolayers). The RDE studies on 30 wt% Pt*/ACCS indicated a shift in Pt–OH formation of 40 mV when compared with

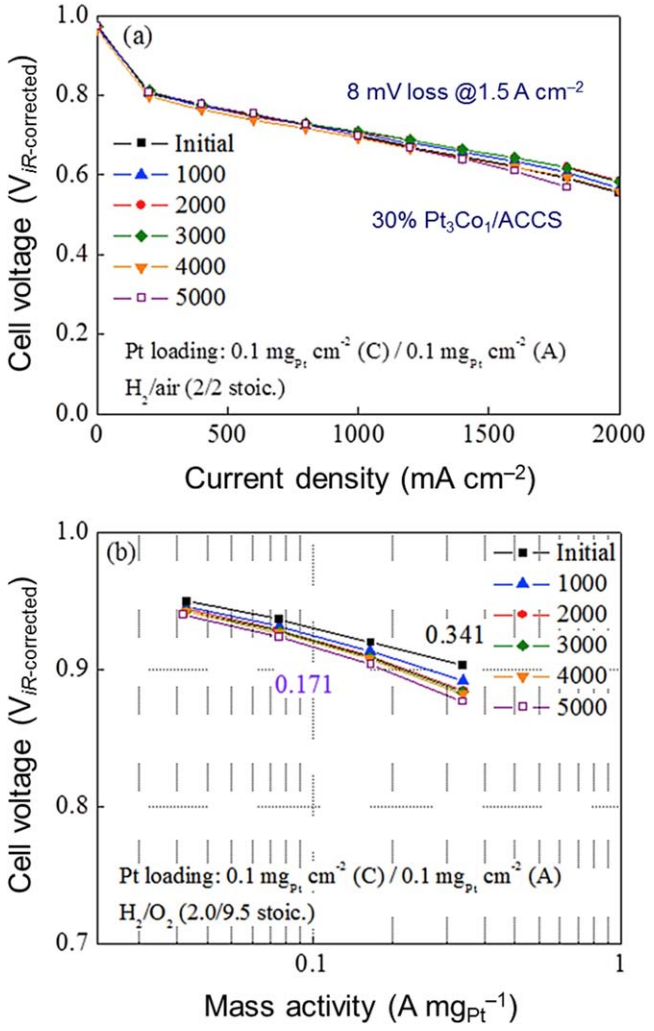

Figure 18. Supports stability test for Pt*/ACCS (1.0–1.5 V potential cycling for 5,000 cycles): (a) H_2/air performance and (b) MA. Reprint from permission from Ref. 52; Copyright 2016, Elsevier.

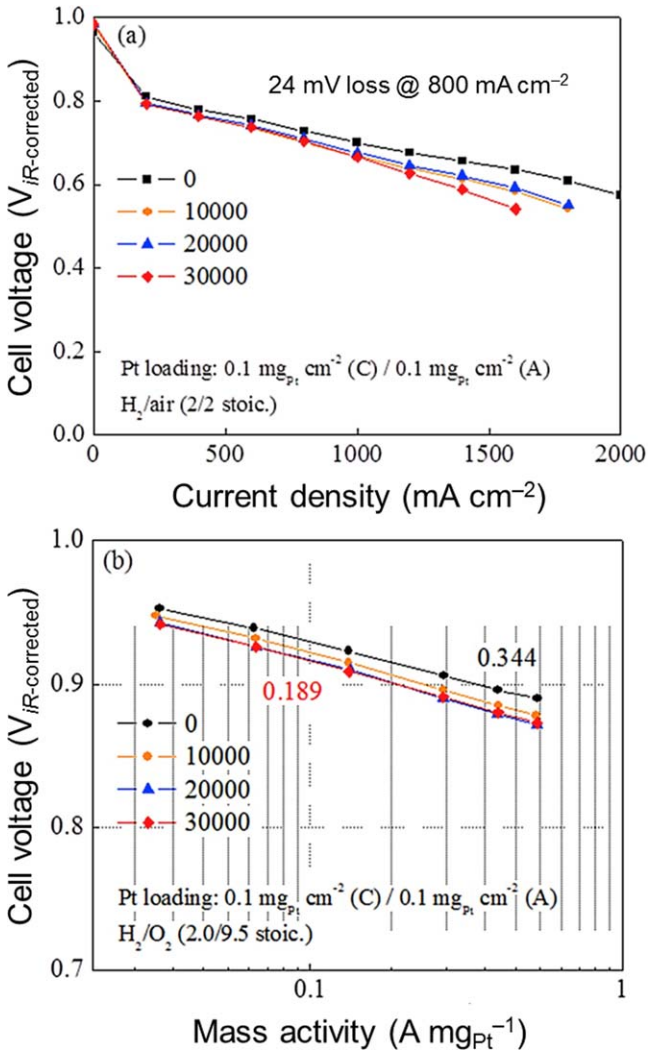

Figure 19. Catalyst stability test for Pt*/ACCS (0.6–1.0 V potential cycling for 30,000 cycles): on (a) H_2/air performance and (b) MA. Reprint from permission from Ref. 52; Copyright 2016, Elsevier.

Pt/C or Pt/ACCS. The potential shift for Pt oxidation to higher values as indicated by the higher open circuit voltage increases the MA in average from 150 to 400 mA mg$_{Pt}^{-1}$, due to the suppression of Pt oxide formation that has much lower exchange current density for ORR (~1.7×10^{-10} A cm^{-2}) when compared to pure Pt (~2.8×10^{-7} A cm^{-2}). During potential cycling between 0.6 and 1.0 V, Pt oxides are formed and reduced according to the following reactions:

$$Pt + H_2O \leftrightarrow PtO + 2H^+ + 2e^- \quad [37]$$

$$Pt + 2H_2O \leftrightarrow PtO_2 + 4H^+ + 4e^- \quad [38]$$

$$Pt + H_2O \leftrightarrow PtO(ads) + 2H^+ + 2e^- \quad [39]$$

Besides higher MA, the Pt*/ACCS catalyst exhibits much higher support and catalyst stability when compared to the pure Pt catalyst. Pt dissolves during potential cycling conditions according to Eqs. 40 and 41:

$$PtO + 2H^+ \rightarrow Pt^{2+} + H_2O \quad [40]$$

$$PtO_2 + 4H^+ + 2e^- \rightarrow Pt^{2+} + 2H_2O \quad [41]$$

Thus, less Pt oxide formation in Pt*/ACCS due to higher Pt oxidation potential alleviates Pt dissolution in the reverse scan and enhances the catalyst stability.

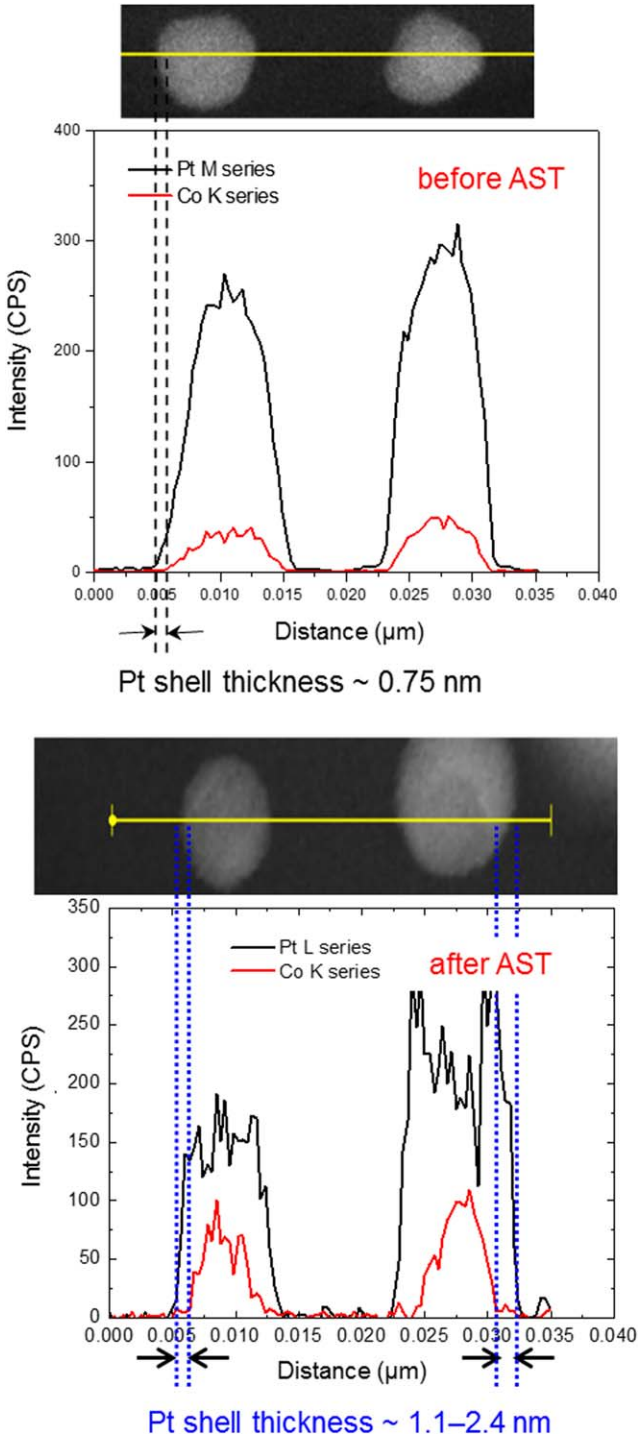

Figure 20. Line scanning compositional analyses of Pt*/ACCS: (a) before and (b) after AST.

Conclusions

The objective of the research was to develop a highly stable ACCS supports as well as a highly active and stable Pt*/ACCS catalysts. Simulation techniques were applied to evaluate the validity of the commonly applied Tafel approximation for the calculation of the MA and SA. A one-dimensional agglomeration model was developed to understand the effects of exchange current density, porosity, agglomerate size, Nafion® film thickness and Pt loading on the MA and SA. A detailed and more precise definition of MA and SA was given to elucidate the variation of MA and SA with the catalyst loading. In the spherical agglomerate model, the surface area per unit volume is regarded as independent of the loading; however, as in the case of the ECSA, it may also depend on the loading and the thickness of the CL. A new non-linear scaling factor was introduced, which considers the effect of the loading on the volumetric agglomerate density. The scaling factor was found to be exponentially dependent on the loading. Finally, the loading dependent Tafel equation was derived, which contains both the utilization and the non-linear scaling factor. The dimensionless penetration depth was identified as the main factor that controls the validity of the application of the kinetic Tafel equation, i.e., when the MA is independent of the catalyst loading. The penetration depth, however, depends on the loading. Consequently, MA and SA are independent of the loading in a certain region only. A new structure parameter was introduced to estimate the real porous structure by using fractal theory. The volumetric catalyst density was corrected by the fractal dimension measured by Hg porosimetry, which gave a good agreement with the experimental values.

The following constraints were addressed when engineering the hybrid Pt*/ACCS catalyst: (i) accomplish chemical and electrochemical stability of the catalyst and the support at high potentials, low pH, and high temperatures; (ii) design an ACCS with an onset potential and kinetic activity similar to that of Pt; (iii) develop highly active and stable Pt shell–Co core catalysts. Chemical and electrochemical stability of the catalyst and the support at high potentials was accomplish by optimizing the hydrophilic/hydrophobic support ratio and the structural properties (amorphous/crystalline ratio). The Pt/ACCS showed no loss in H_2/air performance, indicating excellent support stability with no potential loss after 5,000 cycles. The Pt*/ACCS showed high rated power density (0.174 g_{Pt} kW^{-1}), excellent support stability (8 mV loss at 1,500 mA cm^{-2}), and enhanced catalyst durability (24 mV loss at 800 mA cm^{-2}) under AST conditions. The support stability tests under 1.0–1.5 V cycling conditions showed a potential loss of 8 mV at 1,500 mA cm^{-2}, and an ECSA loss of 22% after 5,000 cycles. The improved catalyst stability of Pt*/ACCS is attributed to a lower formation of Pt oxide, which leads to less dissolution of Pt in the backward scan from 1.0 to 0.6 V. The Pt*/ACCS catalyst which showed high initial performance, good support stability, and good catalyst stability, would be an ideal cathode catalyst candidate for automotive application of PEMFCs.

Acknowledgments

The financial support of the Department of Energy (contract no. DE-FC36–03GO13108 and DE-EE0000460) and the financial support of the National Science Foundation (contract no. 0966956) are acknowledged gratefully.

References

1. H. A. Gasteiger, S. S. Kocha, B. Sompalli, and F. T. Wagner, *Appl. Catal. B: Environ.*, **56**, 9 (2005).
2. R. Makharia, S. S. Kocha, P. T. Yu, M. A. Sweikart, W. Gu, F. T. Wagner, and H. A. Gasteiger, *ECS Trans.*, **1**, 3 (2006).
3. X. Li, H. R. Colón-Mercado, G. Wu, J.-W. Lee, and B. N. Popov, *Electrochem. Solid-State Lett.*, **10**, B201 (2007).
4. J. Wu, X. Z. Yuan, J. J. Martin, H. Wang, J. Zhang, J. Shen, S. Wu, and W. Merida, *J. Power Sources*, **184**, 104 (2008).
5. Y. Sugawara, A. P. Yadav, A. Nishikata, and T. Tsuru, *Electrochem.*, **75**, 359 (2007).
6. P. J. Ferreira, G. J. la O', Y. Shao-Horn, D. Morgan, R. Makharia, S. Kocha, and H. A. Gasteiger, *J. Electrochem. Soc.*, **152**, A2256 (2005).
7. S. Mitsushima, S. Kawahara, K.-I. Ota, and N. Kamiya, *J. Electrochem. Soc.*, **154**, B153 (2007).
8. F. Kodera, Y. Kuwahara, A. Nakazawa, and M. Umeda, *J. Power Sources*, **172**, 698 (2007).
9. R. Borup, J. Davey, F. Garzon, D. Wood, P. Welch, and K. More, *ECS Trans.*, **3**, 879 (2006).
10. V. A. Sethuraman, J. W. Weidner, A. T. Haug, and L. V. Protsailo, *J. Electrochem. Soc.*, **155**, B119 (2008).
11. M. Crum and W. Liu, *ECS Trans.*, **3**, 541 (2006).
12. A. Laconti, H. Liu, C. Mittelsteadt, and R. McDonald, *ECS Trans.*, **1**, 199 (2006).

13. S. D. Knights, K. M. Colbow, J. St-Pierre, and D. P. Wilkinson, *J. Power Sources*, **127**, 127 (2004).
14. L. M. Roen, C. H. Paik, and T. D. Jarvi, *Electrochem. Solid-State Lett.*, **7**, A19 (2004).
15. Y. Shao, G. Yin, J. Zhang, and Y. Gao, *Electrochim. Acta*, **51**, 5853 (2006).
16. B. Avasarala, R. Moore, and P. Haldar, *Electrochim. Acta*, **55**, 4765 (2010).
17. C. J. Tseng, S. T. Lo, S. C. Lo, and P. P. Chu, *Mater. Chem. Phys.*, **100**, 385 (2006).
18. E. Antolini, J. R. C. Salgado, and E. R. Gonzales, *J. Power Sources*, **160**, 957 (2006).
19. L. Xiong, A. M. Kannan, and A. Manthiram, *Electrochem. Commun.*, **4**, 898 (2002).
20. F. H. B. Lima, M. J. Giz, and E. A. Ticianelli, *Braz. Chem. Soc.*, **16**, 328 (2005).
21. N. Travitsky, T. Ripenbein, N. Golodnitsky, Y. Rosenberg, L. Burshtein, and L. Peled, *J. Power Sources*, **161**, 782 (2006).
22. M.-K. Min, J. Cho, K. Cho, and H. Kim, *Electrochim. Acta*, **45**, 4211 (2000).
23. U. A. Paulus, A. Wokaun, G. G. Scherer, T. J. Schmidt, V. Stamenkovic, V. Radmilovic, N. M. Markovic, and P. N. Ross, *J. Phys. Chem. B*, **106**, 4181 (2002).
24. V. R. Stamenkovic, B. S. Mun, M. Arenz, K. J. J. Mayrhofer, C. A. Lucas, G. Wang, P. N. Ross, and N. M. Markovic, *Nat. Mater.*, **6**, 241 (2007).
25. V. Stamenkovic, B. S. Mun, K. J. J. Mayrhofer, P. N. Ross, N. M. Markovic, J. Rossmeisl, J. Greeley, and J. K. Nørskov, *Angew. Chem. Int. Ed.*, **45**, 2897 (2006).
26. K. Jayasayee, J. A. R. V. Veen, T. G. Manivasagam, S. Celebi, E. J. M. Hensen, and F. A. de Bruijn, *Appl. Catal. B: Environ.*, **111–112**, 515 (2012).
27. P. Mani, R. Srivastava, and P. Strasser, *J. Power Sources*, **196**, 666 (2011).
28. A. S. Aricò, A. K. Shukla, H. Kim, S. Park, M. Min, and V. Antonucci, *Appl. Surf. Sci.*, **172**, 33 (2001).
29. A. K. Shukla, M. Neergat, P. Bera, V. Jayaram, and M. S. Hegde, *J. Electroanal. Chem.*, **504**, 111 (2001).
30. T. Toda, H. Igarashi, H. Uchida, and M. Watanabe, *J. Electrochem. Soc.*, **146**, 3750 (1999).
31. T. Toda, H. Igarashi, and M. Watanabe, *J. Electrochem. Soc.*, **145**, 4185 (1998).
32. V. Stamenković, T. J. Schmidt, P. N. Ross, and N. M. Marković, *J. Phys. Chem. B*, **106**, 11970 (2002).
33. V. R. Stamenkovic, B. Fowler, B. S. Mun, G. Wang, P. N. Ross, C. A. Lucas, and N. M. Marković, *Science*, **315**, 493 (2007).
34. Y. Hoshi, T. Yoshida, A. Nishikata, and T. Tsuru, *Electrochim. Acta*, **56**, 5302 (2011).
35. U. A. Paulus, A. Wokaun, G. G. Scherer, T. J. Schmidt, V. Stamenkovic, N. M. Markovic, and P. N. Ross, *Electrochim. Acta*, **47**, 3787 (2002).
36. Q. Huang, H. Yang, Y. Tang, T. Lu, and D. L. Akins, *Electrochem. Commun.*, **8**, 1220 (2006).
37. M. Pourbaix, in *Atlas of Electrochemical Equilibria in Aqueous Solutions* (Pergamon Press, Oxford) (1966).
38. M. Uchimura and S. Kocha, *ECS Trans.*, **11**, 1215 (2007).
39. R. M. Darling and J. M. Meyers, *J. Electrochem. Soc.*, **150**, A1523 (2003).
40. D. C. Johnson, D. T. Napp, and S. Bruckenstein, *Electrochim. Acta*, **15**, 1493 (1970).
41. K. Kinoshita, J. T. Lundquist, and P. Stonehart, *J. Electroanal. Chem.*, **48**, 157 (1973).
42. K. I. Ota, S. Nishigori, and N. Kamiya, *J. Electroanal. Chem.*, **257**, 205 (1998).
43. Z. Li, R. Zeng, L. Wang, L. Jiang, S. Wang, and X. Liu, *Int. J. Hydrogen Energy*, **41**, 21394 (2016).
44. S. Takahashi, N. Takahashi, N. Todoroki, and T. Wadayama, *ACS Omega*, **1**, 1247 (2016).
45. N. Jung et al., *NPG Asia Mater.*, **8**, e237 (2016).
46. D. Yang, Z. Yan, B. Li, D. C. Higgins, J. Wang, H. Lv, Z. Chen, and C. Zhang, *Int. J. Hydrogen Energy*, **41**, 18592 (2016).
47. M. Vorokhta et al., *Appl. Surf. Sci.*, **365**, 245 (2016).
48. I. Khalakhan, M. Vorokhta, M. Václavu, B. Šmíd, J. Lavková, I. Matolínová, R. Fiala, N. Tsud, T. Skála, and V. Matolín, *Electrochim. Acta*, **211**, 52 (2016).
49. D. S. Choi, A. W. Robertson, J. H. Warner, S. O. Kim, and H. Kim, *Adv. Mater.*, **28**, 7115 (2016).
50. T. Kim and B. N. Popov, *Int. J. Hydrogen Energy*, **41**, 1828 (2016).
51. B. N. Popov, T. Kim, and W. S. Jung, *ECS Tran.*, **85**, 123 (2018).
52. T. Kim, T. Xie, W. S. Jung, and B. N. Popov, *Int. J. Hydrogen Energy*, **42**, 12507 (2017).
53. W. S. Jung and B. N. Popov, *ACS Appl. Mater. Interfaces*, **9**, 23679 (2017).
54. G. Liu, X. Li, and B. N. Popov, *J. Power Sources*, **195**, 6373 (2010).
55. G. Liu, X. Li, P. Ganesan, and B. N. Popov, *Appl. Catal. B: Environ.*, **93**, 156 (2009).
56. G. Liu, X. Li, P. Ganesan, and B. N. Popov, *Electrochim. Acta*, **55**, 2853 (2010).
57. V. Nallathambi, J.-W. Lee, S. P. Kumaraguru, G. Wu, and B. N. Popov, *J. Power Sources*, **183**, 34 (2008).
58. G. Liu, X. Li, J.-W. Lee, and B. N. Popov, *Catal. Sci. Technol.*, **1**, 207 (2011).
59. W. S. Jung and B. N. Popov, *Carbon*, **122**, 746 (2017).
60. H. A. Gasteiger, J. E. Panels, and S. G. Yan, *J. Power Sources*, **127**, 162 (2004).
61. W. S. Jung and B. N. Popov, *Catal. Today*, **295**, 65 (2017).
62. K. Kinsohita, in *Electrochemical Oxygen Technologies* (John Wiley & Sons, New York) (1992).
63. Á. Kriston, T. Xie, D. Gamliel, P. Ganesan, and B. N. Popov, *J. Power Sources*, **243**, 958 (2013).
64. K. C. Neyerlin, R. Srivastava, C. Yu, and P. Strasser, *J. Power Sources*, **186**, 261 (2009).
65. T. Xie, W. Jung, T. Kim, P. Ganesan, and B. N. Popov, *J. Electrochem. Soc.*, **161**, F1489 (2014).
66. F. T. Wagner, B. Lakshmanan, and M. F. Mathias, *J. Phys. Chem. Lett.*, **1**, 2204 (2010).
67. K. F. Blurton, P. Greenberg, H. G. Oswin, and D. R. Rutt, *J. Electrochem. Soc.*, **119**, 559 (1972).
68. M. Peuckert, T. Yoneda, R. A. Dalla Betta, and M. Boudart, *J. Electrochem. Soc.*, **133**, 944 (1986).
69. I. E. L. Stephens, A. S. Bondarenko, U. Grønbjerg, J. Rossmeisl, and I. Chorkendorff, *Energy Environ. Sci.*, **5**, 6744 (2012).
70. M. Nesselberger, S. Ashton, J. C. Meier, I. Katsounaros, K. J. J. Mayrhofer, and M. Arenz, *J. Am. Chem. Soc.*, **133**, 17428 (2011).
71. L. Gan, H. Du, B. Li, and F. Kang, *New Carbon Mater.*, **25**, 53 (2010).
72. M. Inaba, H. Yamada, J. Tokunaga, and A. Tasaka, *Electrochem. Solid-State Lett.*, **7**, A474 (2004).
73. A. Bonakdarpour, T. R. Dahn, R. T. Atanasoski, and M. K. Debe, *Electrochem. Solid-State Lett.*, **11**, B208 (2008).
74. M. Watanabe, H. Sei, and P. Stonehart, *J. Electroanal. Chem.*, **261**, 375 (1989).
75. M. K. Debe, *J. Electrochem. Soc.*, **159**, B54 (2012).
76. M. Lee, M. Uchida, D. A. Tryk, H. Uchida, and M. Watanabe, *Electrochim. Acta*, **56**, 4783 (2011).
77. M. S. Saha, D. Malevich, E. Halliop, J. G. Pharaoh, B. A. Peppley, and K. Karan, *J. Electrochem. Soc.*, **158**, B562 (2011).
78. N. Alonso-Vante, *Chem. Phys. Chem.*, **11**, 2732 (2010).
79. A. Kucernak and S. Chen, *J. Phys. Chem. B*, **108**, 3262 (2004).
80. N. A. Siddique and F. Liu, *Electrochim. Acta*, **55**, 5357 (2010).
81. A. Kriston, T. Xie, and B. N. Popov, *Electrochim. Acta*, **121**, 116 (2014).
82. F. Jaouen, F. Charreteur, and J. P. Dodelet, *J. Electrochem. Soc.*, **153**, A689 (2006).
83. M. Yuasa, A. Yamaguchi, H. Itsuki, K. Tanaka, M. Yamamoto, and K. Oyaizu, *Chem. Mater.*, **17**, 4287 (2005).
84. K. Suzuki and N. Sawai, *J. Electrochem. Soc.*, **151**, A2132 (2004).
85. D. Villers, X. Jacques-Bedard, and J. P. Dodelet, *J. Electrochem. Soc.*, **151**, A1507 (2004).
86. P. Mani, R. Srivastava, and P. Strasser, *J. Phys. Chem. C*, **112**, 2770 (2008).
87. H. Kim, N. P. Subramanian, and B. N. Popov, *J. Power Sources*, **138**, 14 (2004).
88. B. N. Popov, X. Li, G. Liu, and J.-W. Lee, *Int. J. Hydrogen Energy*, **36**, 1794 (2011).
89. H. Angerstein-Kozlowska, in *Comprehensive Treatise of Electrochemistry*, ed. E. Yeager, J. O. M. Bockris, B. E. Conway, and S. Sarangapani (Plenum Press, New York) Vol. 9 (1984).
90. S. Huang, P. Ganesan, and B. N. Popov, *ACS Catal.*, **2**, 825 (2012).
91. S. Huang, P. Ganesan, and B. N. Popov, *Appl. Catal. B: Environ.*, **96**, 224 (2010).
92. S. Huang, P. Ganesan, W. S. Park, and B. N. Popov, *J. Am. Chem. Soc.*, **131**, 13898 (2009).
93. M. Perry, J. Newman, and E. J. Cairns, *J. Electrochem. Soc.*, **145**, 5 (1998).
94. F. Jaouen, G. Lindbergh, and G. Sundholm, *J. Electrochem. Soc.*, **149**, A437 (2002).
95. E. L. Gyenge, *J. Power Sources*, **152**, 105 (2005).
96. Á. Kriston, G. Inzelt, I. Faragó, and T. Szabó, *Comp. Chem. Eng.*, **34**, 339 (2010).
97. W. Suna, B. A. Peppley, and K. Karan, *Electrochim. Acta*, **50**, 3359 (2005).
98. A. Weber and W. Yoon, *J. Electrochem. Soc.*, **158**, B1007 (2011).
99. G. Lin, D. Hong-da, L. Bao-hua, and K. Fei-yu, *New Carbon Mater.*, **25**, 53 (2010).
100. J. Z. Zhang, K. Hongsirikarn, and J. G. Goodwin Jr, *J. Power Sources*, **196**, 7957 (2011).
101. P. Gode, F. Jaouen, G. Lindbergh, A. Lundblad, and G. Sundholm, *Electrochim. Acta*, **48**, 4175 (2003).
102. A. Kriston, T. Xie, P. Ganesan, and B. N. Popov, *J. Electrochem. Soc.*, **160**, F406 (2013).
103. J. L. Perez Bernal and M. A. Bello, *Appl. Surf. Sci.*, **185**, 99 (2001).
104. J. Ihonen, F. Jaouen, G. Lindbergh, A. Lundblad, and G. Sundholm, *J. Electrochem. Soc.*, **149**, A448 (2002).
105. S. Martin, P. L. Garcia-Ybarra, and J. L. Castillo, *Int. J. Hydrogen Energy*, **35**, 10446 (2010).
106. S. Martin, P. L. Garcia-Ybarra, and J. L. Castillo, *J. Power Sources*, **195**, 2443 (2010).
107. A. A. Kulikovsky, *Electrochim. Acta*, **55**, 6391 (2010).
108. M. Secanell, K. Karan, A. Suleman, and N. Djilali, *Electrochim. Acta*, **52**, 6318 (2007).
109. S. Litster and N. Djilali, *Electrochim. Acta*, **52**, 3849 (2007).
110. A. J. Bard and L. R. Faulkner, in *Electrochemical Methods* (John Wiley & Sons, New York) 2nd ed. (2001).
111. G. Y. Inzelt, *J. Solid State Electrochem.*, **15**, 1373 (2011).
112. W. Jung, T. Xie, T. Kim, P. Ganesan, and B. N. Popov, *Electrochim. Acta*, **167**, 1 (2015).
113. T. Kim, T. Xie, W. Jung, F. Gadala-Maria, P. Ganesan, and B. N. Popov, *J. Power Sources*, **273**, 761 (2015).
114. E. Antolini, *Appl. Catal. B Environ.*, **88**, 1 (2009).
115. *DOE cell component accelerated stress test protocol for PEM fuel cells* (2007), http://www1.eere.energy.gov/hydrogenandfuelcells/pdfs/component_durability-prfile.pdf.
116. A. Liyama, S. Iguchi, A. Daimaru, and K. Shinohara, *Fuel Cell Commercialization Conference of Japan* (2007).
117. A. Liyama, S. Iguchi, A. Daimaru, and K. Shinohara, *Fuel Cell Commercialization Conference of Japan* (2011).

118. A. Ohma, K. Shinohara, A. Ohma, A. Liyama, T. Yoshida, and A. Daimaru, *ECS Trans.*, **41**, 775 (2011).
119. Y. Hashimasa, Y. Matsuda, and T. Shimizu, *Electrochim. Acta*, **179**, 119 (2015).
120. C. A. Reiser, L. Bregolia, T. W. Patterson, J. S. Yi, J. D. Yang, and M. L. Perry, *Electrochem. Solid State Lett.*, **8**, A273 (2005).
121. T. W. Patterson and R. M. Darling, *Electrochem. Solid State Lett.*, **9**, A183 (2006).
122. Y. C. Park, K. Kakinuma, M. Uchida, D. A. Tryk, T. Kamino, and H. Uchida, *Electrochim. Acta*, **91**, 195 (2013).
123. Y. Sugawara, T. Okayasu, A. P. Yadav, A. Nishikata, and T. Tsuru, *J. Electrochem. Soc.*, **159**, F779 (2012).
124. U.S. DRIVE Fuel Cell Technical Team Roadmap, *U.S. DRIVE Fuel Cell Technical Team Roadmap*, p. 13, http://energy.gpv./sites/rod/files/2014/02/f8/fctt_roadmap_june2013.pdf (2013).
125. R. Mukundan, "Accelerated Testing Validation." *U.S. DOE FCT Program AMR and Peer Evaluation Meeting*, p. 11, https://hydrogen.energy.gov/pdfs/review14/fc016_mukundan_2014_o.pdf (2014).
126. W. S. Jung and B. N. Popov, *ACS Sustainable Chem. Eng.*, **5**, 9809 (2017).
127. P. Strasser et al., *Nat. Chem.*, **2**, 454 (2010).
128. F. Tao, M. E. Grass, Y. Zhang, D. R. Butcher, J. R. Renzas, Z. Liu, J. Y. Chung, B. S. Mun, M. Salmeron, and G. A. Somorjai, *Science*, **322**, 932 (2008).
129. S. Alayoglu and B. Eichhorn, *J. Am. Chem. Soc.*, **130**, 17479 (2008).
130. Y.-N. Wu, S.-J. Liao, H.-F. Guo, and X.-Y. Hao, *J. Power Sources*, **224**, 66 (2013).
131. X.-Z. Fu, Y. Liang, S.-P. Chen, J.-D. Lin, and D.-W. Liao, *Catal. Commun.*, **10**, 1893 (2009).
132. Y. Cho, W. H. Lee, and H. Kim, *J. Mater. Chem. A*, **2**, 11635 (2014).